Dalton Transactions

ROYAL SOCIETY OF CHEMISTRY

PAPER

View Article Online
View Journal | View Issue

Cite this: *Dalton Trans.*, 2025, **54**, 11262

Engineering an amine-functionalized Zn(II) interpenetrated metal–organic framework for comprehensive iodine uptake across diverse phases and selective azo dye adsorption†

Shaikh Arfa Akmal,[a] Mohd Khalid, *[a] M. Shahid [a] and Musheer Ahmad [b]

In this study, a two-fold interpenetrated 3D Zn-based metal–organic framework, $\{[Zn_2(btc)(Hata)(H_2O)_2]\}_n$ (AR-2), was successfully synthesized *via* a hydrothermal approach using 1,2,4,5-benzene tetracarboxylic acid and 3-amino-1,2,4-triazole as oxygen and nitrogen donor ligands, respectively. Single-crystal X-ray diffraction (SCXRD) analysis reveals the presence of two distinct Zn nodes (Zn1 and Zn2) adopting tetrahedral and square-pyramidal geometries, confirmed by the τ geometric index. The topological analysis identifies a 3D bbf-3,4-Cccm net. Thorough analysis using elemental analysis, FT-IR, PXRD, TGA, SEM, EDS, and TEM demonstrates the robust structural integrity of AR-2. The framework of AR-2 possesses numerous π-electron-rich rings and accessible nitrogen donor sites, which significantly enhance its adsorption efficiency for iodine and azo dyes. It demonstrates remarkable iodine uptake across vapor, aqueous, and organic phases, with an uptake capacity of 828 mg g^{-1} (dry, 75 °C) and 415 mg g^{-1} (dry, 25 °C). At the same time, under humid conditions, it captures 523 mg g^{-1} (75 °C) and 131 mg g^{-1} (25 °C). AR-2 also achieves 89–91% iodine adsorption in aqueous and organic solvents. Remarkably, iodine-loaded AR-2 retains up to 96–97% of its captured iodine at 25 °C, demonstrating its potential for long-term storage and safe transportation of radioiodine. Furthermore, AR-2 selectively adsorbs hazardous azo dyes, such as Bismarck Brown and Methyl Orange, from aqueous solutions, showcasing rapid kinetics, high stability, and reusability. These findings position AR-2 MOF as a promising candidate for environmental remediation, including off-gas filtration and wastewater treatment in nuclear and chemical industries.

Received 26th May 2025,
Accepted 19th June 2025

DOI: 10.1039/d5dt01228g

rsc.li/dalton

1. Introduction

In recent decades, the energy sector has shifted towards nuclear power as an alternative to limited coal reserves.[1] Developed nations prioritize energy security by reducing their dependence on imported fossil fuels, especially after recent coal shortages.[2,3] Nuclear energy offers a powerful solution, providing extremely high energy output and a low carbon footprint.[4,5] This makes it a promising way to tackle the global energy crisis while reducing carbon dioxide emissions, a major contributor to global warming.[6–8] However, nuclear reactors generate various harmful and volatile radioactive elements. Managing these radioactive byproducts, like iodine isotopes (^{129}I and ^{131}I), ^{85}Kr, ^{99}Tc, and ^{3}H, has become a major area of research. ^{129}I and ^{131}I are generated as byproducts during the nuclear fission of uranium and plutonium.[9–12] When used nuclear fuel (UNF) is treated with concentrated nitric acid (HNO_3) for reprocessing, iodide ions are oxidized into volatile iodine gas, which can easily escape into off-gas streams. Since ^{129}I has a half-life of over 10 million years, any atmospheric release could cause long-term environmental contamination.[13] Radioactive iodine is especially dangerous because it dissolves easily in water and spreads quickly through the environment.[14] When people are exposed to radioactive iodine, it accumulates in the thyroid gland, increasing the risk of thyroid cancer and posing significant health risks, especially with prolonged or high-level exposure. Historical events like the Chernobyl disaster showed a sharp increase in thyroid cancer cases, especially in children, after iodine exposure. Even consuming excessive natural iodine (over 1.1 mg day^{-1}) can harm thyroid function and lead to cancer.[15–17] Given these serious risks to human health and the

[a]*Functional Inorganic Materials lab (FIML), Department of Chemistry, Aligarh Muslim University, Aligarh 202002, India. E-mail: khalid215@gmail.com*
[b]*Department of Applied Chemistry, ZHCET, Aligarh Muslim University, Aligarh 202002, India*

†Electronic supplementary information (ESI) available. CCDC 2430163. For ESI and crystallographic data in CIF or other electronic format see DOI: https://doi.org/10.1039/d5dt01228g

environment, quickly and effectively capturing iodine is a critical research goal.[18–20]

At the same time, water pollution caused by harmful chemicals like organic azo-dyes poses another serious threat to ecosystems. Most industries discharge wastewater into water bodies, often released without proper treatment, introducing toxic chemical dyes into rivers and lakes. Studies estimate that over 100 000 commercial dyes exist, with over 10 000 tonnes dumped into water bodies yearly.[21,22] Azo dyes, including alkaline, acid, reactive, direct, and dispersive types, are widely found in wastewater from industries such as textiles, leather, paper, printing, and cosmetics.[23,24] Although these dyes enhance the colorfulness of materials, they account for up to 40% of dye pollution in developing nations like India and Bangladesh.[25] Natural dyes break down more readily, whereas azo dyes are significantly more stable, making them commonly used in food processing.[26] Extensive evidence suggests that azo dyes are carcinogenic and mutagenic, with the potential to cause respiratory diseases.[27] Therefore, the removal of azo dyes from water is essential. Several approaches, including physical, chemical, and biological treatments, have been investigated for their elimination.[28–30] Common azo dyes include Trypan Blue, Lithol Red, Orange I, Orange II, 4-Phenylazo-Naphthylamine, Methyl Red, Allura Red, Sunset Yellow, Yellow AB, Carmoisine, Mercury Orange, and Phenylazophenol, along with their reduced aromatic amines. However, the degradation, decolorization, and reduction of these dyes can produce toxic and mutagenic byproducts.[25] Thus, it is important to find simple and inexpensive procedures for their removal.[31] Several effective techniques are available for adsorbing iodine and dyes, including sodium filtration, anion-exchange resins, flocculation–precipitation, extraction, and adsorption methods.[32] Among the available methods, adsorption is preferred for its low cost, simple operation, and environmental friendliness.[33] Metal–organic frameworks (MOFs) have recently emerged as promising materials for adsorbing radioactive iodine and dyes.[34,35] The presence of secondary building units (SBUs) offers a flexible design strategy to create MOFs with durable and multifunctional properties.[36,37] In this work, using two different ligands in a one-pot mixed-ligand approach allows for better framework tuning and the introduction of accessible sites for guest interactions. The primary linker selected for this study is a rigid, aromatic, polycarboxylate oxygen (O) donor ligand, 1,2,4,5-benzene tetracarboxylic acid (H_4btc). Its diverse coordination modes contribute to forming stable secondary building units (SBUs) during self-assembly, enhancing the overall framework stability.[38,39] As a co-ligand, 3-amino-1,2,4-triazole (Hatz), a nitrogen (N) donor ligand with a high nitrogen content of 66.67%, was chosen due to its ability to form rigid metal–organic complexes, thereby improving structural rigidity and stability[40] and, additionally, Hatz exhibits versatile bridging coordination modes, such as μ1,2, μ2,4, and μ1,2,4.[41] These ligands have been widely used to construct functional, high-density energetic frameworks with abundant π-electron-rich rings and NH_2 groups responsible for the excellent adsorption properties.[42] These features empower AR-2 to efficiently capture radioactive iodine in vapor and liquid phases while selectively adsorbing toxic dyes from wastewater. Specifically, AR-2 shows strong selectivity for cationic Bismarck Brown (BB) through electrostatic interactions with its negatively charged framework. Meanwhile, it captures anionic Methyl Orange (MO) *via* hydrogen bonding and π–π stacking interactions. The nitrogen-rich sites in AR-2 further enhance iodine adsorption, while the interpenetrated structure adds mechanical stability, even under harsh conditions.

2. Experimental methods

2.1. Chemicals and procedures

Solvents and analytical-grade reagents were used without additional purification. 1,2,4,5-Benzene tetracarboxylic acid (H_4btc), 3-amino-1,2,4-triazole (Hata), $Zn(NO_3)_2{\cdot}4H_2O$, and KOH were purchased from Sigma-Aldrich.

2.2. Physical measurements

Characterization of AR-2 was carried out using various techniques. The structural features were analyzed by FTIR spectroscopy with KBr pellets on a PerkinElmer Spectrum GX spectrophotometer (400–4000 cm^{-1}). Elemental composition (C, H, and N) was determined at the Micro-Analytical Laboratory, CDRI, Lucknow, India. The electronic spectrum was recorded using a PerkinElmer λ-45 UV-visible spectrophotometer, with 1 cm path length cuvettes. The crystallinity and phase purity were confirmed through PXRD measurements using a Miniflex II diffractometer with Cu-Kα radiation. Thermal stability was assessed *via* TGA (TGA-50H) at a heating rate of 20 °C min^{-1} from 25 to 800 °C. Raman spectra were acquired with a HORIBA Scientific LabRAM series instrument at a 785 nm excitation wavelength. Morphological features were observed using SEM (Quanta FEG 250) and TEM (JEOL-JEM-2100 at 200 kV). The zeta potential was measured with JS94H micro iontophoresis apparatus. Surface composition and oxidation states were analyzed by XPS (Thermo Fisher Nexsa) with an Al Kα source, in a vacuum of $\sim 10^{-8}$ mbar, with a pass energy of 200 eV, a dwell time of 10 ms, and a binding energy range of 0–1350 eV. The solid-state electronic spectrum of AR-2 was obtained using a PerkinElmer λ-850 UV-visible spectrophotometer with a universal reflectance accessory.

2.3. Single-crystal X-ray diffraction analysis

The crystal structure of AR-2 was determined using a Bruker SMART APEX CCD diffractometer at 100 K with graphite-monochromated Mo-Kα radiation (λ = 0.71073 Å).[43] Data integration and reduction were processed using the SAINT software,[44] and the space group was identified through XPREP.[45] Empirical absorption corrections were applied with SADABS.[46] Structural refinement on F^2 was performed using least-squares techniques within the OLEX-2 program package.[47] Non-hydrogen atoms were refined anisotropically, while hydrogen atoms were

placed in calculated positions and refined isotropically. The CCDC reference number for AR-2 is 2430163.†

2.4. Synthesis of AR-2: $[Zn_2(btc)(Hata)(H_2O)_2]_n$

A mixture of $Zn(NO_3)_2{\cdot}4H_2O$ (0.2 mmol, 0.066 g), 1,2,4,5-benzene tetracarboxylic acid (H_4btc) (0.2 mmol, 0.044 g), 3-amino-1,2,4-triazole (Hata) (0.1 mmol, 0.023 g), and KOH (1 mmol, 0.0561 g) was dissolved in 5 mL of double-distilled water and stirred for 15 minutes. The solution was then transferred into a 10 mL Teflon-lined stainless-steel autoclave and heated at 120 °C for three days. Upon slow cooling to room temperature, fine, well-formed, colorless crystals suitable for single-crystal XRD analysis were obtained (yield 69.8%). Melting point 351 °C, anal. calcd (%) for $C_{12}H_{10}N_4O_{10}Zn_2$, C = 28.77; H = 2.01; N = 11.18; found: C = 28.84; H = 2.05; N = 11.12. FT-IR (KBr, cm^{-1}): 3375 (s), 1605 (s), 1548 (s), 1384 (m), 1071 (s), 607 (w), 498 (w).

2.5. Iodine adsorption and release

2.5.1. Iodine capture in the vapor phase under dry conditions. A 30 mg sample of AR-2 was placed in a 5 mL glass vial to evaluate iodine capture in the vapor phase under dry conditions and at high temperatures. The vial, along with the sample, was accurately weighed, and the initial weight was noted. It was then positioned inside a larger 20 mL glass vial containing solid iodine crystals. The larger vial was heated to 75 °C at 1.0 bar in a preheated oven. At regular time intervals, the small vial containing AR-2 was taken out, its outer walls were cleaned to remove any residue, and the weight was recorded before placing it back.

The same procedure was followed for iodine capture at room temperature (25 °C) without applying heat.

The iodine uptake capacity (q) was calculated using eqn (1).

$$q = \frac{w_2 - w_1}{w_1} \quad (1)$$

Here, w_1 is the weight of the vial with the sample at the beginning and w_2 is the weight after the iodine capture experiment.

2.5.2. Iodine capture in the vapor phase under humid conditions. To investigate iodine capture in the vapor phase under humid conditions and high temperatures, 30 mg of AR-2 was placed in a 5 mL glass vial. The vial and sample were weighed and noted. This vial was then set inside a larger 20 mL glass vial and placed in a glass chamber containing solid iodine crystals. An open 5 ml glass vial filled with water was also placed inside the glass chamber to create a humid environment. The same setup was used for a control experiment to measure moisture adsorption by AR-2 without iodine, but the chamber did not contain iodine crystals.

The glass chamber was heated to 75 °C at 1.0 bar in a preheated oven. The small vial containing AR-2 was removed regularly, its outer walls were thoroughly cleaned, and its weight was measured before being returned to the setup.

2.5.3. Iodine release from I_2@AR-2 in the vapor phase. To evaluate iodine release, 20 mg of iodine-loaded MOF (I_2@AR-2) was heated in an open glass vial at 125 °C under 1.0 bar pressure using an oil bath. The release efficiency (RE) of iodine was determined using eqn (2).

$$\mathrm{RE} = \left(\frac{20 - W_t}{W_x}\right) \times 100 \quad (2)$$

Here, W_t is the AR-2 weight at time t and W_x represents the weight of iodine adsorbed in 20 mg of I_2@AR-2.

2.5.4. Recycling of AR-2 in the vapor phase. Iodine-loaded AR-2 was regenerated by heating at 125 °C, followed by sequential washing with methanol and hexane until the washings (filtrate) became colorless. The material was then purified for 24 hours using a Soxhlet extractor containing methanol.

2.5.6. Iodine adsorption from water (aqueous solution). For the initial study, 30 mg of the activated sample was added to 5 mL of a 200 ppm aqueous iodine solution and stirred continuously. After 48 hours, the remaining iodine in the solution was determined by titration using a standardized sodium thiosulfate (hypo) solution. The same experiment was repeated for a saturated aqueous iodine solution, and the obtained sample was designated as I_2@AR-2.

2.5.7. Iodine removal from organic solution. A stock solution of iodine in cyclohexane of 200 ppm was prepared for the experiment. A 20 mg sample of activated AR-2 was added to 50 mL of an iodine solution in cyclohexane and stirred. Every hour for up to 13 hours, a 3 mL sample was taken and centrifuged, and the clear liquid was analysed using UV-vis spectroscopy to monitor adsorption.

2.5.8. Iodine release study. A 10 mg sample of iodine-loaded AR-2 was placed in methanol, and the release process was monitored by measuring absorbance using UV-vis spectroscopy at different time intervals.

2.6. Dye adsorption experiment

For the dye adsorption study, 20 mg of AR-2 was added to 100 mL of a 10 ppm aqueous dye solution (BB or MO) and stirred continuously. Samples were taken every 5 minutes for the first to third reading, and the remaining readings were recorded after 10 minutes up to 40 minutes and analyzed using UV-vis spectroscopy in the 200–800 nm range. The pH of the solution was adjusted with 0.1 M HCl or 0.1 M NaOH. Equilibrium adsorption capacities were determined using standard methods and calibration curves. The following equations calculated the adsorption capacity (q_t) and removal efficiency (R).

Adsorption capacity (q_t) – eqn (3)

$$q_t = \frac{(C_i - C_t)V}{m} \quad (3)$$

The adsorption capacity, q_t (mg g^{-1}), is determined using the following parameters: V represents the volume of the solution (L), m is the mass of the adsorbent (mg), C_i is the initial concentration of the adsorbate (mg L^{-1}), and C_t is the concentration (mg L^{-1}) at a given time (t).

Removal efficiency (%) – eqn (4)

$$\%\,\text{Removal efficiency}\,(R) = \frac{C_0 - C_t}{C_0} \times 100 \quad (4)$$

where C_0 = initial concentration (mg L^{-1}) and C_t = concentration (mg L^{-1}) at time t. The adsorption performance of AR-2 was evaluated through UV-visible analysis, with additional investigations into the effects of pH and temperature on adsorption behavior.

3. Results and discussion

3.1. Synthesis strategy

Researchers have widely adopted a mixed-ligand approach, using polycarboxylic acids and nitrogen-donor ligands, to synthesize novel MOFs with diverse applications.[48] In this study, we synthesized a two-fold interpenetrated 3D MOF, AR-2, using Zn(II), 1,2,4,5-benzene tetracarboxylic acid, and 3-amino-1,2,4-triazole *via* a simple hydrothermal method. The resulting framework, $\{[Zn_2(btc)(Hata)(H_2O)_2]\}_n$, features the interpenetrated structure, π-electron-rich rings, and abundant $-NH_2$ groups from the 3-amino-1,2,4-triazole ligand which endow AR-2 with excellent adsorption properties.[42] In AR-2, Hata binds to Zn(II) ions through two of its nitrogen atoms in a bridging fashion to make the frame very intact and robust and contribute to forming an interconnected 3D network. In contrast, the remaining nitrogen (N2 and N4) atoms remain uncoordinated. These free nitrogen atoms act as electron-rich donor sites, facilitating host–guest interactions and enhancing the adsorption efficiency of iodine; plenty of rings in the framework and surface charge on AR-2 are responsible for dye adsorption. The synthesis process is depicted in Scheme 1.

3.2. SCXRD structural analysis of AR-2

Single-crystal X-ray analysis confirms that AR-2 adopts a monoclinic crystal system with the space group $P2_1/n$. The crystallographic data and refinement details are summarized in Table 1, while key bond lengths and angles are provided in Tables S1 and S2.† The asymmetric unit (Fig. 1a) of AR-2 contains two crystallography-independent Zn(II) ions, one btc^{4-} ligand, one Hatz, and two water molecules. Thus, the chemical formula of the complex was written as $\{[Zn_2(btc)(Hata)(H_2O)_2]\}_n$. The interesting feature of AR-2 is the Zn atoms, *i.e.*, Zn1 and Zn2, present in the structure with two distinct coordination environments as shown in Fig. 1b. In AR-2, each Zn1(II) ion (Fig. 2a) adopts a four-coordinate environment, bonding with two carboxylate oxygen atoms (O2 and O6) from two distinct btc^{4-} ligands, one oxygen (O10) from a coordinated water molecule, and one nitrogen (N1) from the Hata ligand. The Zn–O/N bond lengths vary between 1.9374 and 2.0058 Å. In

Table 1 Crystal data and structure refinement of AR-2

Identification code	AR-2
Empirical formula	$C_{12}H_{10}N_4O_{10}Zn_2$
Formula weight	501.03
Temperature/K	293(2)
Crystal system	Monoclinic
Space group	$P2_1/n$
a/Å	10.2462(2)
b/Å	14.8595(2)
c/Å	10.8233(2)
α/°	90
β/°	101.383(2)
γ/°	90
Volume/Å^3	1615.47(5)
Z	4
ρ_{calc}/g cm^{-3}	2.0598
μ/mm^{-1}	3.038
F(000)	1002.8
Crystal size/mm^3	0.47 × 0.23 × 0.14
Radiation	Mo Kα (λ = 0.71073)
2θ range for data collection/°	4.72 to 54.78
Index ranges	$-12 \le h \le 13$, $-18 \le k \le 18$, $-13 \le l \le 13$
Reflections collected	26 956
Independent reflections	3463 [R_{int} = 0.0325, R_{sigma} = 0.0233]
Data/restraints/parameters	3463/0/260
Goodness-of-fit on F^2	1.042
Final R indexes [$I \geq 2\sigma(I)$]	R_1 = 0.0236, wR_2 = 0.0565
Final R indexes [all data]	R_1 = 0.0287, wR_2 = 0.0581
Largest diff. peak/hole/e Å^{-3}	0.46/−0.47

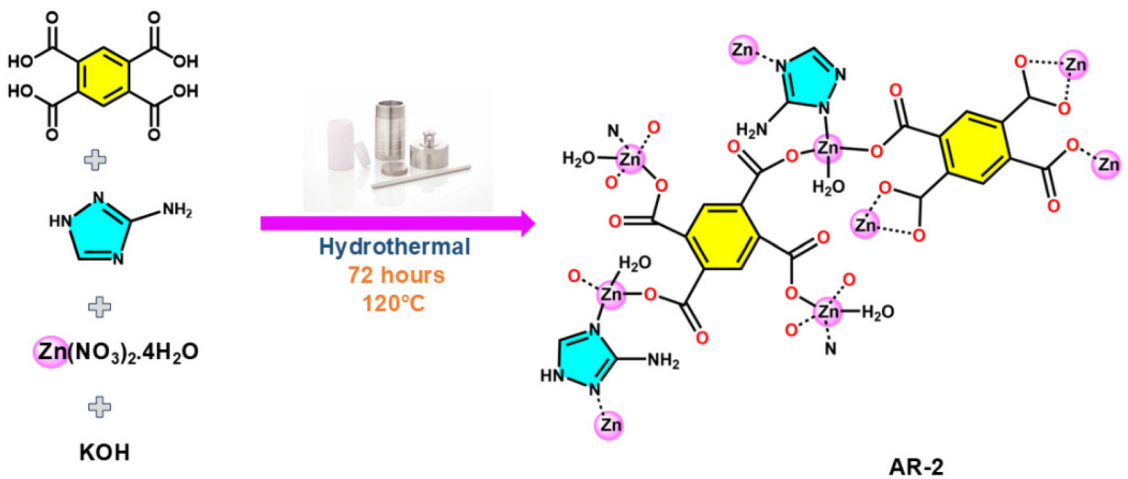

Scheme 1 Synthetic route to AR-2 (Zn-based MOF).

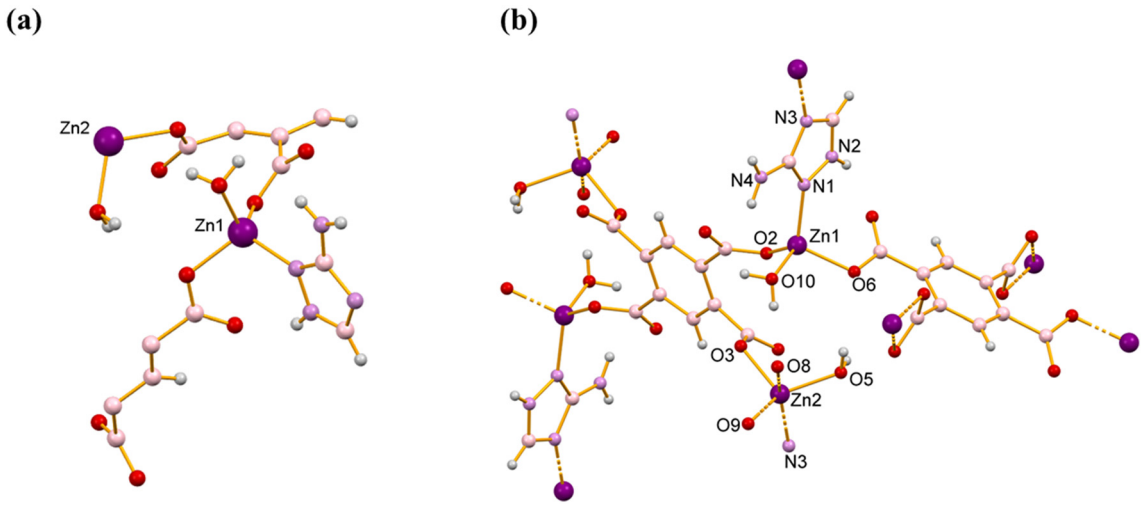

Fig. 1 (a) Asymmetric unit representation of AR-2. (b) X-ray crystal structure of $\{[Zn_2(btc)(Hata)(H_2O)_2]_n\}$.

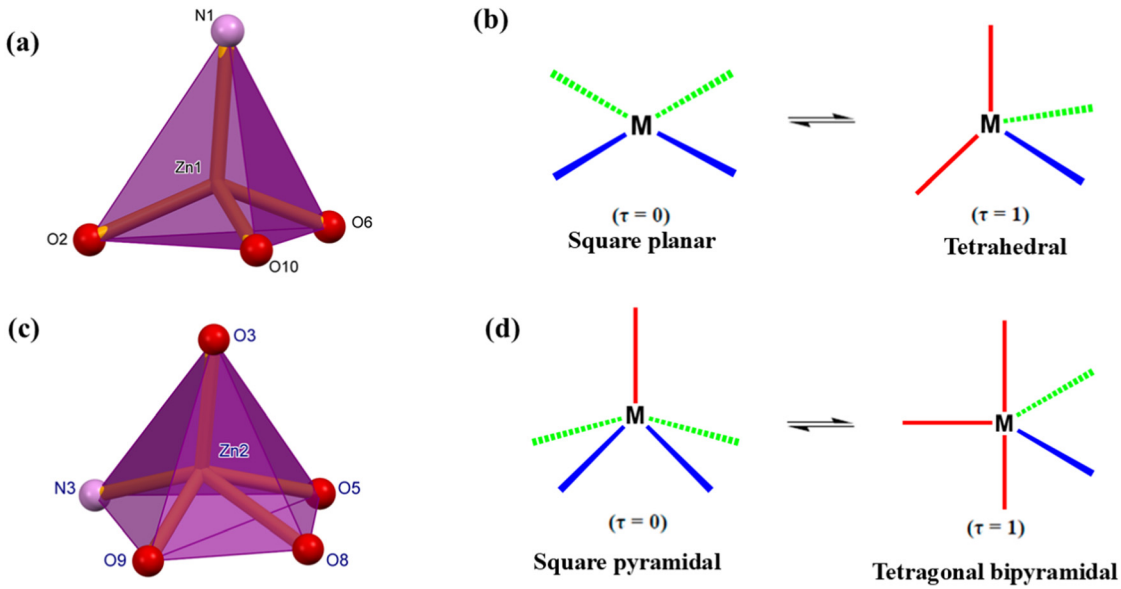

Fig. 2 (a) Distorted tetrahedral geometry of the Zn1 center with coordination to N1, O2, O6, and O10. (b) Geometric transition from square planar (τ = 0) to tetrahedral (τ = 1). (c) Distorted square pyramidal geometry of the Zn2 center with coordination to O3, N3, O5, O8, and O9. (d) Geometric transition from square pyramidal (τ = 0) to tetragonal bipyramidal (τ = 1).

four-coordinate systems, both square planar and tetrahedral geometries are possible. The structural geometry is determined using the 4-coordination geometry index $\{\tau_4 = [360 - (\alpha + \beta)]/141\}$, where α and β represent the largest valence angles around the coordination center. A τ_4 value of 0 indicates a square planar configuration, whereas a value of 1 suggests a tetrahedral geometry (Fig. 2b).[49] Since the calculated tau value for Zn1 is τ_4 = 1, it can be said that the geometry of Zn1 is tetrahedral and this is also confirmed by the passing of the plane through N1, Zn1, and O10, which is perpendicular to the plane passing through O6, Zn1, and O2 (Fig. S1†). The bond angles around the Zn1 atom, such as N1–Zn1–O6 at 109.55(7)°, N1–Zn1–O10 at 104.65(7)°, O10–Zn1–O2 at 113.06 (7)°, and O2–Zn1–O6 at 106.76(7)°, indicate a distorted tetrahedral geometry.[50] In contrast, the Zn2 coordination environment (Fig. 2c) consists of five coordination sites, including one nitrogen (N3) from its ligand Hata, one oxygen (O5) from a coordinated water molecule, and three oxygen atoms (O3, O8, and O9) from the carboxylate groups of two different btc^{4-} ligands. A five-coordinated system can adopt either a trigonal bipyramidal (tbp) or square pyramidal (sq-py) geometry. To differentiate these geometries, Addison *et al.* introduced the τ parameter,[51] which ranges from 0 to 1, where values closer to 0 indicate a square pyramidal geometry and those near 1

correspond to a trigonal bipyramidal geometry (Fig. 2d). The τ parameter is calculated as $(\beta - \alpha)/60$, where α and β are the two largest bond angles at the coordination center. For Zn2, with α = 146.30° and β = 127.79°, the calculated τ_5 value is 0.30, confirming a distorted square pyramidal geometry.[52] To further confirm the distorted square pyramidal geometry, Zn2, O8, O5, O9, and N3 form a quasi-square plane, with O3 positioned at the apex (Fig. S2†). The key bond angles measured include O9–Zn2–N3 at 99.00(7)°, O5–Zn2–N3 at 97.62(7)°, O8–Zn2–O5 at 85.47(7)°, O8–Zn2–O9 at 55.45(7)°, O3–Zn2–O8 at 89.39(7)°, O3–Zn2–O9 at 104.11(7)°, O3–Zn2–O5 at 108.94(7)°, and O3–Zn2–N3 at 120.54(7)°. The bond valence analysis[53] shows that Zn1 and Zn2 have slightly higher bond valence sums of 2.45 and 2.30, respectively, which are close to the expected +2 oxidation state of Zn. This confirms the structural integrity of their coordination environments. Additionally, the calculated bond valences for the coordinating oxygen and nitrogen atoms align well with the typical Zn(II) coordination chemistry. Several Zn-based crystal structures incorporating H_4btc or Hata ligands have been reported in the literature, exhibiting comparable Zn–O and Zn–N bond lengths but differing in coordination modes and geometries around the Zn(II) ion.[54,55] The btc^{4-} anions in AR-2 exhibit two distinct μ4-bridging modes (Fig. 3a & b). In one mode, all four carboxylate groups adopt an $(\eta^1\text{-}\eta^0)\text{-}(\eta^1\text{-}\eta^0)\text{-}(\eta^1\text{-}\eta^0)\text{-}(\eta^1\text{-}\eta^0)\text{-}\mu^4$ *syn*-monodentate configuration, while in the other, the groups follow an $(\eta^1\text{-}\eta^0)\text{-}(\eta^1\text{-}\eta^1)\text{-}(\eta^1\text{-}\eta^0)\text{-}(\eta^1\text{-}\eta^1)\text{-}\mu^4$ arrangement.[56] Among these, two carboxylate groups follow the *syn*-monodentate mode, and the other two adopt an asymmetric chelating mode (Fig. S3†), as confirmed by the bond lengths (O8–Zn2 = 2.574 and O9–Zn2 = 1.999). The btc^{4-} anions connect adjacent Zn(II) centers through two distinct coordination modes, forming a 2D $[Zn_4(btc)]_n$ network. When viewed overall, the structure exhibits a well-defined 2D architecture, as shown in Fig. S4.† Focusing on a single layer reveals a clear sheet-like arrangement, with each btc^{4-} anion bridging Zn(II) centers in an organized manner. This demonstrates the capability of btc^{4-} to make layered frameworks with detailed connectivity. The Hata ligands adopt a linear geometry[57] with an $(\eta^1)\text{-}(\eta^0)\text{-}(\eta^1)\text{-}(\eta^0)\text{-}\mu^2$ mode (N1, N3) to connect or flank between the adjacent Zn(II) ions, *i.e.*, Zn1 and Zn2, into an "I"-like shape unit $[Zn_2(Hata)]$ (Fig. 3c). Meanwhile, the N2 and N4 nitrogen atoms remain uncoordinated, allowing them to interact with guest species readily. Based on these connection modes, the 2D $[Zn_4(btc)]_n$ networks are interconnected through them to convert the layers into a more entangled 3D framework (Fig. S5†). Additionally, unusual Zn···π interactions were observed in AR-2, with Zn1···C1 and C6 distances of ~2.750 and 2.740 Å and Zn2···C5, C10, and C12 distances of ~2.692, 2.624, and 2.966 Å, as shown in Fig. S6.† These interactions result from the donation of the Zn(II) lone pair of electrons to the LUMOs of the carbonyl carbon atoms and the carbons in the triazole ring, leading to Zn(lp)···π interactions[58] that significantly contribute to stabilizing the framework by enhancing metal-to-ligand coordination. These interactions are possible because the Zn(II) center acts as an electron donor; at the same time, the carbonyl and triazole ring carbons possess electron-deficient π-systems capable of accepting electron density. In the same way, a lone pair of O8 and O9 donates their electron density to the C8 and C9 of the benzene ring. This cooperative interaction helps maintain the structural stability of AR-2 and enhances its functionality for guest molecules. The stability of the framework is significantly enhanced by many more short contacts that facilitate the connection of adjacent moieties, particularly through hydrogen bonding interactions. In the AR-2 framework, inter-hydrogen bonding is prominently observed between the btc^{4-} anions and water molecules, forming a robust $R_2^2(8)$ hydrogen bonding motif[59] between O6···H5a–O5 (~2.508 Å), O8···H5a–O5 (~2.208 Å), and O8···H10a–O10 (~1.865 Å) (Fig. 4). Moreover, the amine hydrogen of Hata is also involved in inter-hydrogen bonding with the oxygen of the btc^{4-} anion (O9···H4b–N4 ~1.865 Å), further strengthening the network. Moreover, intramolecular hydrogen bonding is also found between N3···H12–C12 (~2.007 Å) and N3···H4b–N4 (~2.555 Å), as shown in Fig. S7.† These intermolecular and intramolecular hydrogen bonds enhance mechanical stability and structural integrity, ensuring durability. A notable C–H···C8(π) interaction[34] is observed between the btc^{4-} units, as illustrated in Fig. 5a, along the *a*-axis. This interaction reveals that the two types of coordination modes of btc^{4-} are effectively bound through these interactions. When viewed along the *c*-axis in Fig. 5b, the framework appears even more compact and closely packed, further highlighting the structural interconnection formed by these interactions. Fig. 6 (a–d) display the structural views of AR-2 along the *c*-axis. The 3D framework arrangement, unit cell packing, and space-

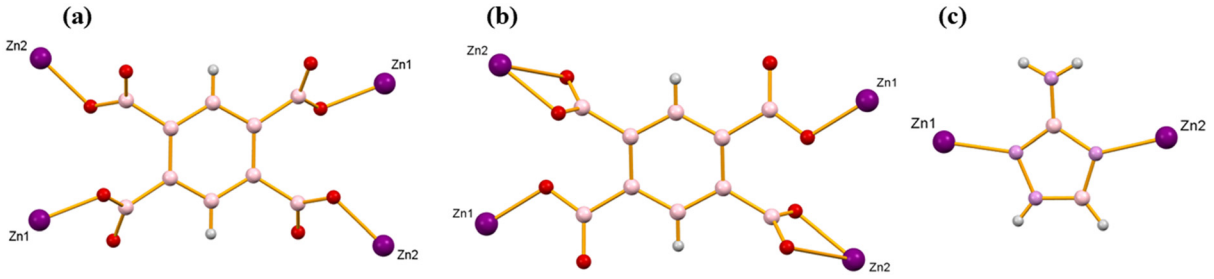

Fig. 3 (a–c) Coordination mode of btc^{4-} and the Hata ligand in AR-2.

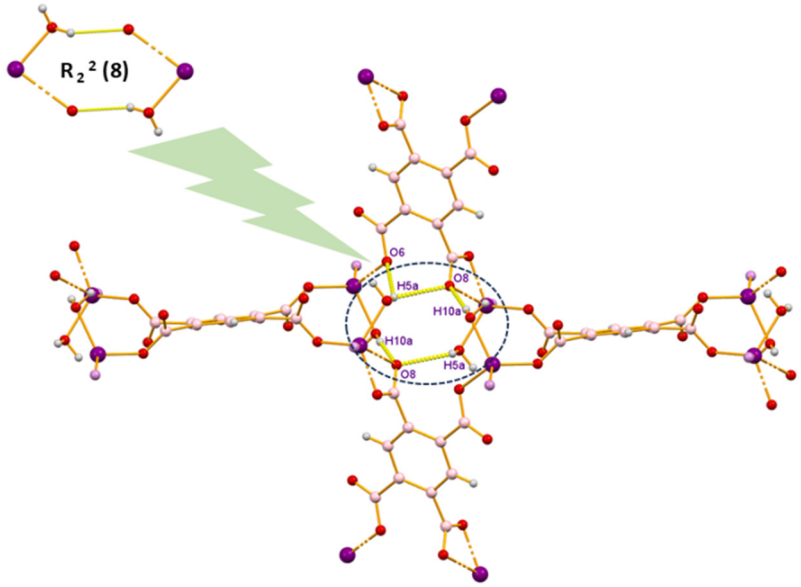

Fig. 4 A view of the hydrogen bonding interactions in AR-2, showing the R_2^2 (8) motif.

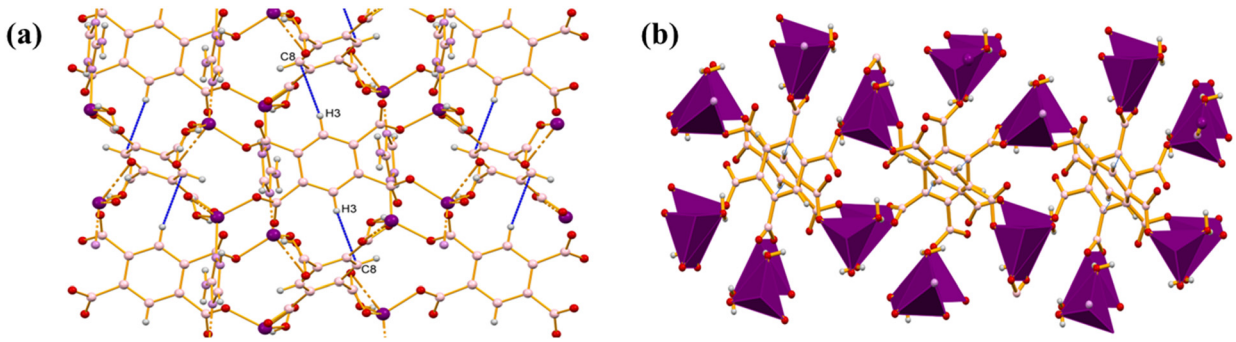

Fig. 5 Illustration of C3–H3···C8(π) interactions between the two different btc^{4-} modes in the AR-2 framework along the *a*-axis (a), revealing a compact structure along the *c*-axis (b).

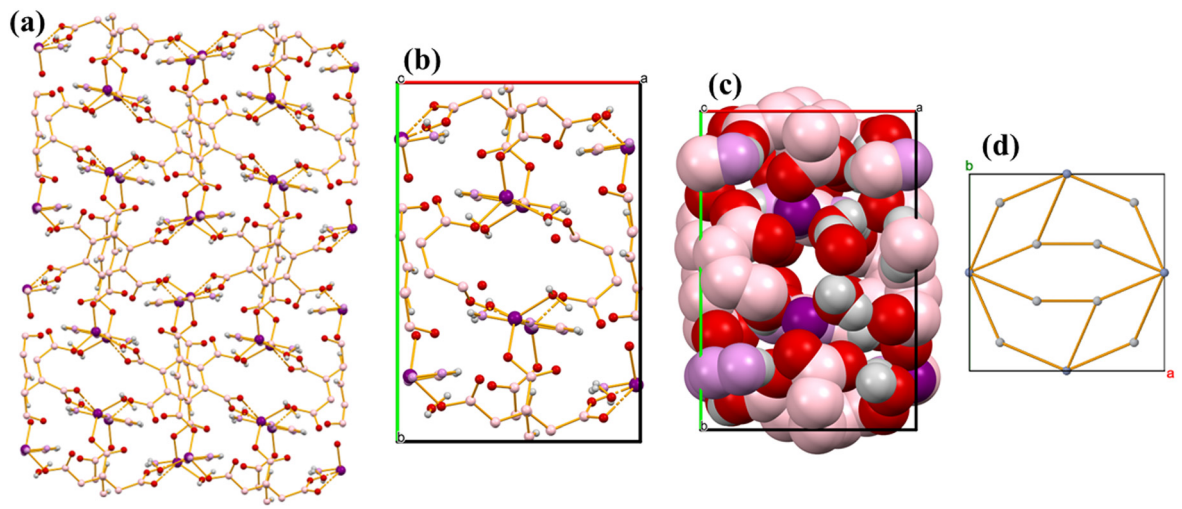

Fig. 6 Structural view of AR-2 along the *c*-axis: (a) 3D view showing the framework arrangement. (b) Packing of the unit cell. (c) Space-filling model of the unit cell. (d) Topological view of the unit cell.

filling model illustrate molecular distribution and guest occupancy, and additionally, topological analysis using Topos-Pro reveals a *sur* topology with a *bbf*-3,4-*Cccm* network in the unit cell, highlighting node-linker connectivity in its 3D network with the same topology (Fig. S8a†), and a polyhedral representation along the *c*-axis further emphasizes the structural organization and connectivity of the framework (Fig. S8b†). Furthermore, the single crystal of AR-2 features repeated stacking of 2D layers (Fig. 7a) and interpenetrated networks (Fig. 7b), resulting in a high-density MOF with ρ = 2.0598 g cm^{-3}.

This interpenetration enhances structural compactness and provides additional interaction sites for guest molecules, a key characteristic of interpenetrated MOFs,[60] which enhances their ability to trap and adsorb guest molecules effectively. This dense framework makes AR-2 particularly suitable for applications involving selective adsorption or capture, where strong interactions with guest molecules are crucial.

3.3. FTIR, TGA, UV-DRS, PXRD, SEM, and TEM analyses of AR-2

The FTIR spectrum of AR-2 exhibits distinct peaks in both the functional group and fingerprint regions (4000–400 cm^{-1}), corresponding to the primary (btc^{4-}) and auxiliary (Hata) ligands. Notably, it provides insights into ligand binding modes. As shown in Fig. 8a, strong to medium-intensity bands appear in the overlapping region of 3410–3350 cm^{-1}, attributed to the asymmetric stretching vibrations of O–H from coordinated water and N–H from the Hata ligand. These bands also indicate the participation of N–H···O hydrogen bonds, as

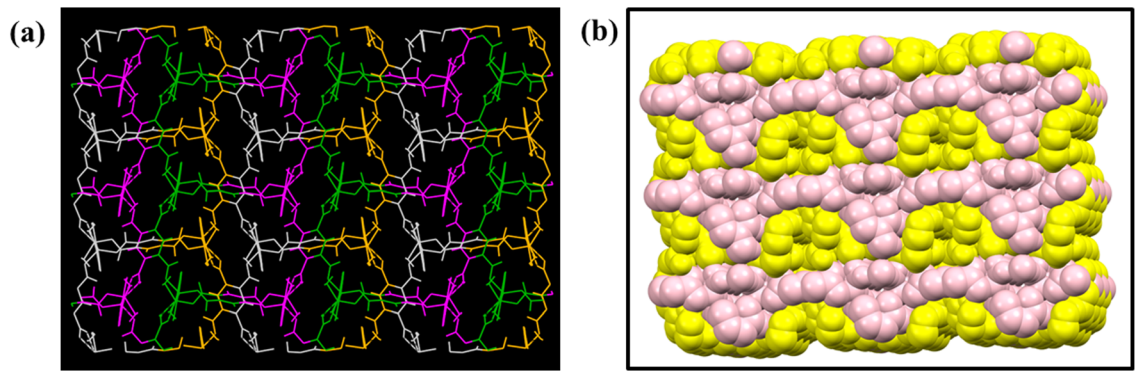

Fig. 7 (a) 3D supramolecular structure of AR-2 constructed from 2D stacking units, with 2D chains highlighted in different colors. (b) Two-fold parallel interpenetrating packing diagram viewed along the *c*-axis.

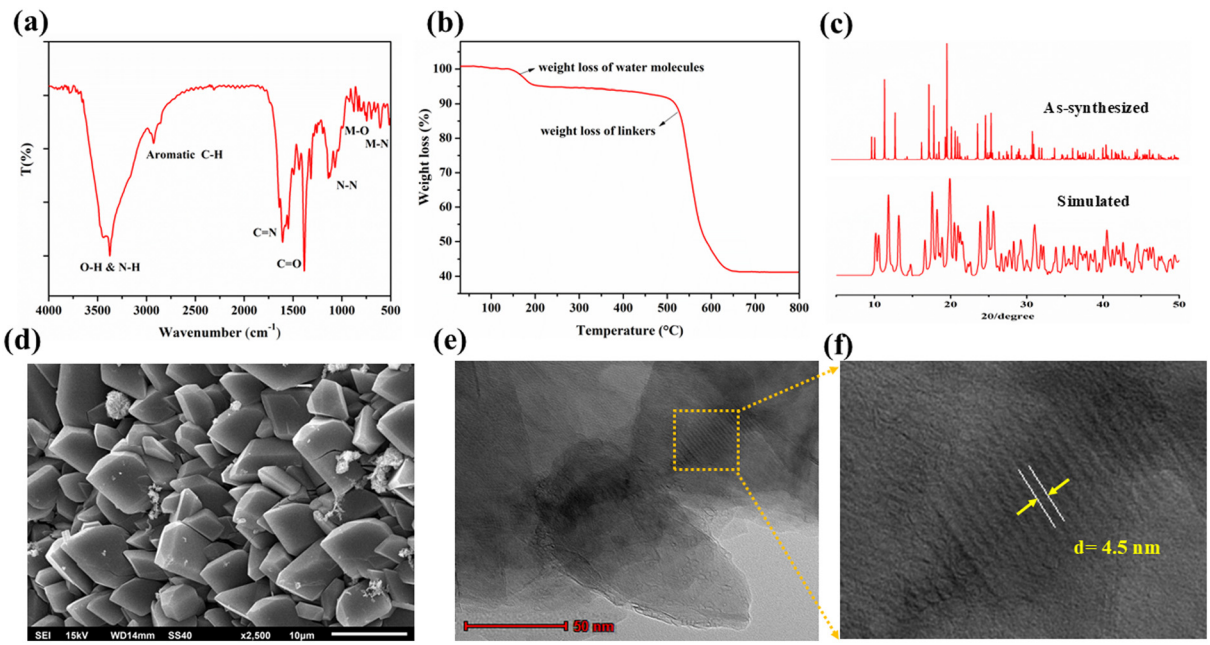

Fig. 8 (a) FT-IR spectrum of AR-2, (b) TGA curve of AR-2, (c) PXRD pattern comparing simulated and as-synthesized AR-2, (d) SEM image of AR-2, and (e & f) TEM images of AR-2 nanostructures.

supported by the extensive hydrogen-bonding network observed in the crystal structure. N–H stretching vibrations align with charge balance analysis, confirming that Hata remains neutral.[61,62] Hydrogen bonding typically induces a shift in vibrational frequencies by weakening the X–H bonds (*e.g.*, O–H, N–H) through interactions with hydrogen bond acceptors, leading to redshifts in their stretching vibrations. For instance, O–H stretching vibrations shift to lower frequencies, typically in the 3200–3600 cm^{-1} range (from free O–H at ~3700 cm^{-1}), while N–H stretching modes shift and broaden due to hydrogen bonding. Additionally, the delta (δ) and gamma (γ) vibrational modes in the 880–1350 cm^{-1} region further support the presence of a robust hydrogen-bonding network in AR-2, underscoring its structural and spectroscopic attributes.[63] The weak-intensity bands at 3110 and 2925 cm^{-1} correspond to the asymmetric stretching vibrations of aromatic C–H in Hata and btc^{4-} ligands.[64] The absence of a peak at 1725 cm^{-1} confirms the complete deprotonation of the H_4btc ligand.[65] Additionally, strong to medium-intensity bands at 1605 cm^{-1} and 1385 cm^{-1}, corresponding to the asymmetric (overlapping with triazole vibrations) and symmetric stretching vibrations of the carboxylate (COO^-) group, indicate coordination of the btc^{4-} moiety to the metal ion in the framework.[55] These bands help identify the carboxylate coordination modes, where the difference between $\nu_{asym}(COO^-)$ and $\nu_{sym}(COO^-)$ determines the binding nature. A $\Delta\nu$ value between 200 and 300 cm^{-1} suggests monodentate coordination, while a lower value (<200 cm^{-1}) implies polydentate or chelating modes.[66] In AR-2, the carboxylate groups of btc^{4-} exhibit $\Delta\nu$ values of approximately 221 cm^{-1} and 160 cm^{-1}, indicating symmetric monodentate and bidentate coordination, respectively. Furthermore, medium-to-strong bands at 1640, 1430, and 1071 cm^{-1} correspond to the stretching vibrations of C=N, C–N, and N–N in the triazole ring.[67–70] Strong absorptions at 876 cm^{-1} and 698 cm^{-1} are assigned to the O–H and C–H bending modes, respectively.[67] Additionally, the absorption peak at 607 cm^{-1} corresponds to Zn–O vibrations, while a weak-intensity band at 498 cm^{-1} is attributed to Zn–N vibrations.[55] Fig. 8b shows the TGA spectrum, confirming the thermal stability of the AR-2 framework up to 180 °C. The TGA profile of AR-2 reveals an initial weight loss occurring between 180 and 200 °C, attributed to the removal of two coordinated water molecules. This is supported by the observed weight loss of 4.5%, aligning closely with the calculated value of 5.1%, and is consistent with the expected release of crystal water molecules from the structure.[54] The compound remains thermally stable up to 550 °C, after which the decomposition of the btc^{4-} and Hata ligands occurs in the 550–600 °C range. Although TGA-IR analysis was not performed, the thermal decomposition behaviour indicates the probable release of gases such as CO_2, nitriles (C≡N), and NH_3, which are typically associated with the degradation of the organic ligand components. The weight loss in this step is 67.5%, which aligns with the calculated value of 71.0%, confirming the expected stepwise degradation of the framework. The remaining residue, 28.0% (TGA obs), corresponds to the formation of ZnO (calcd. 28.9%), consistent with the anticipated thermal decomposition pathway of the material. The UV-vis diffuse reflectance spectrum of AR-2, measured in the 200–800 nm range (Fig. S9†), displays a prominent absorption peak at 304 nm, attributed to ligand-centered (π–π*) electronic transitions within the conjugated framework of btc^{4-} and Hata ligands.[71] Furthermore, the analysis of the experimental and simulated PXRD spectra (Fig. 8c) of AR-2 shows well-defined diffraction peak positions, confirming that AR-2 is a pure phase without impurities. The variations in peak intensities are attributed to the preferential alignment of the crystals.[72] The SEM image of AR-2 (Fig. 8d) reveals a smooth, well-defined block-shaped morphology with sharp edges.[73] Meanwhile, carbon-coated Cu TEM grids for TEM imaging (Fig. 8e) illustrate nanosized AR-2, with high homogeneity in the shape and size of block-shaped crystals with thin, transparent regions, indicative of the 2D morphology of the 3D interpenetrated framework. The lattice fringes showed the presence of well-resolved periodic fringes (Fig. 8f). These analyses attest to the successful delamination of the bulk MOF material into a few-layered material. These findings align with the PXRD results, further validating the crystalline nature of AR-2.[74]

3.4. Iodine adsorption

3.4.1. Vapourised iodine capture under dry, humid, and ambient conditions. The distinctive structure of AR-2, carefully designed with abundant heteroatoms, polar sites, and a significant quantity of π-rich benzene units, inspired us to investigate its potential for iodine vapor capture and storage. As a preliminary step, the chemical stability of AR-2 was evaluated by immersing it in acidic (1 M aqueous HCl) and basic (1 N aqueous NaOH) solutions for 24 hours. The amine-linked AR-2 demonstrated impressive chemical stability, maintaining its structural integrity, as confirmed by PXRD analysis (Fig. S10†). In a UNF reprocessing plant, iodine exists as iodide (I^-) in spent fuel. During fuel dissolution in hot nitric acid, nitrates oxidize iodide to elemental iodine (I_2), which sublimates due to high temperatures, making it a major component of the dissolver off-gas (DOG) stream. At this reprocessing stage, only a small portion of iodine remains as iodide (I^-) in the dissolver solution. Additionally, the DOG stream contains water vapor, emphasizing the need for efficient adsorbents capable of capturing iodine vapor under humid conditions. For experimental studies, the nonradioactive isotope ^{127}I was used as a substitute for radioactive iodine isotopes (^{131}I or ^{129}I) due to laboratory handling limitations.[34]

The iodine vapor uptake capacity of AR-2 under static dry conditions was evaluated, with experimental details provided in Section 2.5.1. The setup was placed in a preheated oven at 75 °C, mimicking the temperature of the dissolver solution during spent fuel reprocessing. Over time, AR-2 adsorbed iodine vapor, and periodic weighing confirmed sorption equilibrium after 48 hours. The maximum iodine uptake capacity under these conditions was 828 mg g^{-1} (Fig. 9a), surpassing several reported MOFs (Table S3†). Since the dissolver off-gas (DOG) stream also contains significant humidity,[42] additional

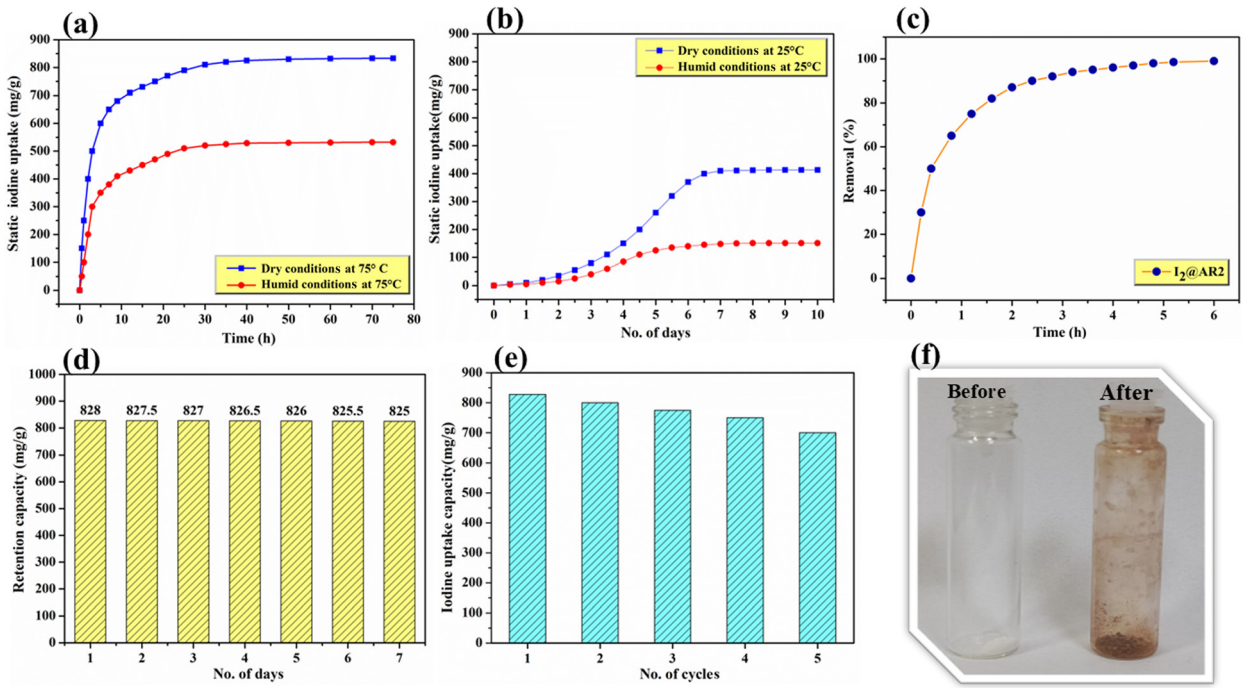

Fig. 9 (a) Static iodine uptake plot of AR-2 at 75 °C under dry and humid conditions. (b) Static iodine uptake plot of AR-2 at 25 °C under dry and humid conditions. (c) Iodine released from I_2@AR-2 upon heating. (d) Iodine retention profile of AR-2. (e) Reusability of AR-2. (f) Image of AR-2 before and after iodine capture at 75 °C under dry conditions.

static adsorption tests were conducted under humid conditions (Section 2.5.2). At 75 °C, AR-2 retained a high iodine uptake capacity of 532 mg g^{-1} (Fig. 9a). Given that off-gas streams in nuclear fuel reprocessing can cool to ambient temperatures,[75] further adsorption experiments were performed at 25 °C. The slower sublimation rate at this temperature resulted in gradual iodine capture, reaching saturation in 7–8 days. The maximum uptake at ambient temperature was 415 mg g^{-1} (Fig. 9b), again outperforming several other MOFs (Table S4†). Under humid conditions at 25 °C, AR-2 exhibited an iodine uptake capacity of 131 mg g^{-1} (Fig. 9b). These findings demonstrate that AR-2 exhibits strong potential for iodine vapor capture across various static adsorption conditions.

3.4.2. Iodine removal and retention capacity in a vapor phase. Desorption was facilitated by heating the sample at 125 °C or soaking it in polar solvents such as methanol (details of the thermal release procedure are mentioned in Experimental section 2.5.3). Within the first 2 hours of heating, approximately 80% of the adsorbed iodine was released, increasing to around 98% (Fig. 9c). However, complete iodine release was unattainable, likely due to certain iodine species being deeply embedded within the AR-2 framework.

To evaluate the iodine retention ability of AR-2 at room temperature, iodine-loaded AR-2 was kept in an open vial under ambient conditions. As shown in Fig. 9d, only 2–3% of the mass was lost after seven days of exposure. This highlights the effectiveness of AR-2 in securely storing and transporting radioactive iodine generated during spent nuclear fuel reprocessing. Its recyclability was investigated to assess the practicality of AR-2 as an iodine adsorbent. Effective release of trapped iodine (I_2@AR-2) is essential and achievable through simple heating or immersion in suitable solvents. The regenerated adsorbent retained structural integrity and was successfully used for up to four cycles of iodine sorption and desorption (Fig. 9e). A distinct color change in AR-2 was also observed, transitioning from white to dark brown, indicating iodine adsorption, as seen in Fig. 9f.

3.4.3. Iodine uptake in aqueous solutions. Even though strict safety rules exist for industries that use radioactive materials, much waste still leaks into oceans and rivers. This radioactive waste, including iodine, can harm aquatic animals and may be dangerous to other living things.[76] There are many studies on capturing iodine from the air, but only a few focus on removing it from water. This is likely because the materials used for adsorption often become unstable in water, or water molecules interfere with the adsorption process, reducing efficiency. Therefore, removing iodine from water is a crucial area of scientific research. AR-2 demonstrates excellent stability in water, making it suitable for aqueous iodine adsorption studies.[77] Since iodine (I_2) has low solubility in water, potassium iodide (KI) was added to facilitate dissolution, forming a triiodide (I_3^-) solution, the most stable polyiodide species in aqueous media.[78] In the experiment, 30 mg of AR-2 was introduced into a 50 mL aqueous solution containing 200 ppm iodine, prepared using a saturated KI solution. This setup maintained a continuous iodine supply due to the equilibrium between I_3^- and (I_2 + I^-), where iodide (I^-)

enhances iodine solubility in water. The mixture was left undisturbed for 48 hours to ensure sufficient interaction between the MOF and iodine. The residual iodine was quantified *via* iodometric titration (details in the ESI, Fig. S11†), indicating 90.4% removal.

3.4.4. Iodine uptake in cyclohexane solutions. The AR-2 framework, composed of btc^{-4} and Hata ligands, features electron-rich rings and free nitrogen donor atoms, enhancing its potential for iodine adsorption. To investigate the iodine adsorption efficiency of the AR-2 framework, model solutions were prepared by dissolving iodine in cyclohexane at concentrations of 200, 150, 100, 50, 25, and 12.5 ppm. Cyclohexane was chosen as the solvent due to its inertness and compatibility with iodine, ensuring reliable analysis. These concentrations were chosen to evaluate the maximum adsorption potential of AR-2 under practical conditions. UV-vis spectra of iodine solutions were measured to generate a calibration curve (Fig. 10a) and track iodine levels before and after adsorption. At room temperature, 20 mg of fresh AR-2 crystals were added to a cyclohexane solution of iodine (200 mg L^{-1}).

Over time, the deep pink color of the solution gradually faded to near colorless, indicating efficient iodine adsorption by the AR-2 network. The adsorption process was analyzed using a UV-visible spectrophotometer, where the absorption band at 522 nm confirmed the presence of iodine in cyclohexane, as depicted in Fig. 10b. The steady decrease in iodine solution absorbance over time, as shown in Fig. 10c, demonstrated the ability of AR-2 to adsorb iodine effectively, reaching equilibrium after 13 hours. The absorption capacity and removal efficiency of AR-2 are further quantified (using eqn (3) and (4)) by regular measurements of the remaining iodine concentration in the solution. As depicted in Fig. 10c and d, the iodine adsorption process by AR-2 was initially rapid. Within the first 3 hours, the adsorption capacity reached 150 mg g^{-1}, corresponding to a removal efficiency of 38.76%. Over the next 6 hours, the adsorption continued steadily, achieving a 320 mg g^{-1} capacity at the 9th hour, indicating a trend toward equilibrium. Finally, after 13 hours, the adsorption process stabilized, reaching equilibrium. At this point, the maximum adsorption capacity of AR-2 was recorded at 356.01 mg g^{-1}, with an optimal iodine removal efficiency of 91.01% (Table S5†).

3.4.5. Adsorption kinetics of iodine in cyclohexane. The adsorption kinetics was analyzed to gain insight into the mechanism and iodine transfer at the solid–solution interface. Both pseudo-first-order and pseudo-second-order models were applied to describe iodine uptake from cyclohexane over time.

The Lagergren pseudo-first-order kinetic model, widely used for liquid–solid adsorption systems, was employed, with its linearized mathematical expression provided in eqn (5).

$$\log(q_e - q_t) = \log q_e - \frac{k_1 \times t}{2.303} \quad (5)$$

The Lagergren pseudo-second-order kinetic model indicates that the adsorption kinetics is governed by the availability of active sites on the adsorbent surface. The process is predominantly controlled by chemical interactions between the adsor-

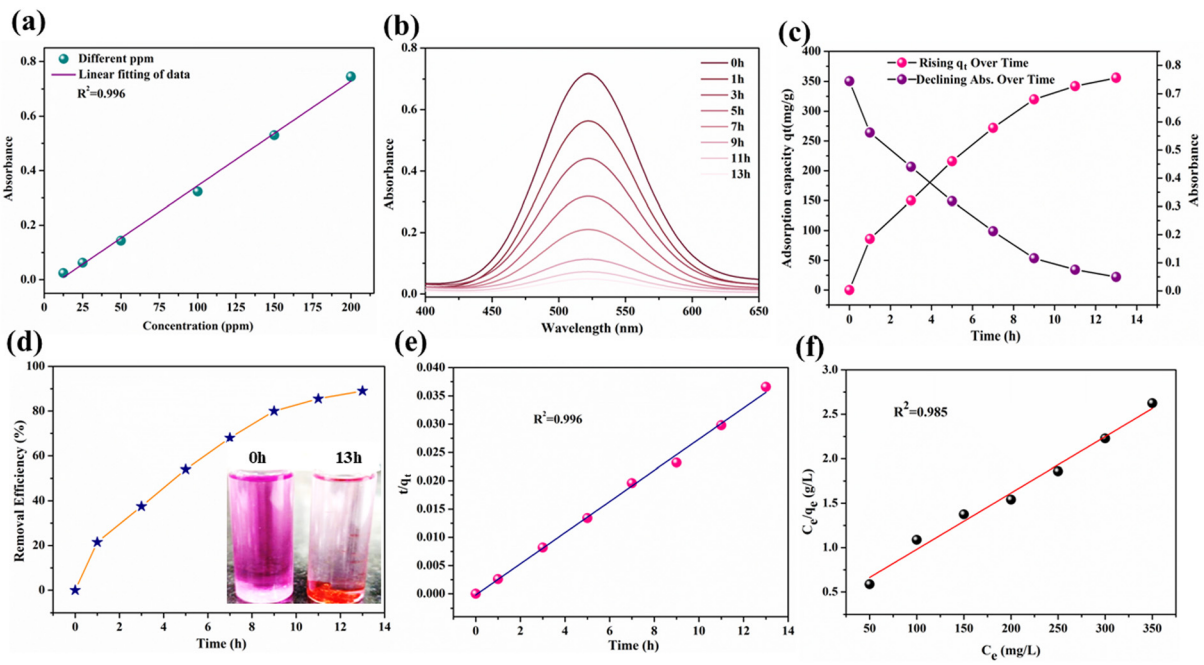

Fig. 10 (a) Linear fit of the standard curve at varying concentrations before adsorption. (b) UV spectra show AR-2 adsorbs iodine (200 ppm) in cyclohexane solution at different intervals. (c) Over time, iodine adsorption by 20 mg of AR-2 in cyclohexane showed increased adsorption with a gradual decrease in absorbance. (d) Time-dependent iodine removal by 20 mg of AR-2 from a saturated cyclohexane solution. (e) Pseudo-second-order kinetic plot for iodine adsorption in cyclohexane. (f) Langmuir isotherm model for iodine uptake by AR-2.

bate and adsorbent at these specific sites. The linearized equation of the model is represented as eqn (6).

$$\frac{t}{q_t} = \frac{1}{(k_2 \times q_e^2)} + \frac{t}{q_e} \quad (6)$$

Here, in this model, q_e (mg g^{-1}) refers to the adsorption capacity at equilibrium, while q_t (mg g^{-1}) indicates the adsorption capacity at a specific time t. The rate constant K_1 (min^{-1}) for the pseudo-first-order model is derived from the slope of the plot of $\log(q_e - q_t)$ against time (Fig. S12a†). Although the correlation coefficient (R^2) was close to 1, the graph showed deviations from linearity, and the adsorption capacity values did not match the calculated ones (Table S6†). This suggests that the model is not suitable for explaining the adsorption kinetics. The rate constant K_2 (g $(mg^{-1}\ min^{-1})^{-1}$) for the pseudo-second-order model is determined from the slope of the t/q_t *versus* time plot (Fig. 10e). The graph shows excellent linearity with an R^2 value of 0.996, confirming that this model accurately represents the iodine adsorption behavior of AR-2, indicating a chemisorption-driven process. However, the adsorption capacity of AR-2 in solution is lower than in the vapor phase, likely due to solvent encapsulation effects restricting iodine interaction with adsorption sites.[79]

3.4.6. Adsorption isotherm. The adsorption of iodine from a cyclohexane solution onto AR-2 at 298 K increases with rising iodine concentration. However, once a certain concentration is reached, the adsorption capacity remains constant, indicating saturation. The adsorption data were evaluated using the Langmuir and Freundlich isotherm models, represented by eqn (7) and (8), to gain deeper insights into the adsorption characteristics and equilibrium behaviour.[80]

$$\frac{C_e}{q_e} = \frac{1}{K_L q_m} + \frac{C_e}{q_m} \quad (7)$$

$$\ln q_e = \ln K_F + \frac{1}{n} \ln C_e \quad (8)$$

Here, the equilibrium concentration (C_e, mg L^{-1}) refers to the concentration at equilibrium, while the adsorption capacity of AR-2 (q_e, mg g^{-1}) represents the amount of adsorbate per gram of adsorbent. The maximum adsorption capacity (q_m, mg g^{-1}) is determined experimentally, and K_L (L mg^{-1}) is the Langmuir equilibrium constant. The Freundlich constant (K_F, [(mg g^{-1}) (L mg^{-1})$1/n$]) represents the adsorption capacity, with the exponent (n) indicating the adsorption intensity. The correlation coefficient (R^2) in Table S7† shows that the Langmuir model (Fig. 10f) better fits the data than the Freundlich model (Fig. S12b†).[81] At 298 K, the theoretical maximum adsorption capacity (298.03 mg g^{-1}) is close to the experimental value (350.06 mg g^{-1}), suggesting that iodine adsorption follows the Langmuir model with a monolayer adsorption mechanism.[82]

3.4.7. Iodine removal and reusability in methanol. Iodine release experiments were conducted by stirring I_2@AR-2 samples in methanol at room temperature (298 K). The methanol gradually changed from colourless to yellowish-brown, indicating iodine release from I_2@AR-2. The extent of release was monitored by UV-vis spectra of the methanol at intervals (Fig. 11a). Bands at 291 and 359 nm correspond to polyiodide ions, and the band at 223 nm is due to I_2.[83] Within minutes, the intensity of these bands increased and then levelled off, indicating equilibrium. These results show rapid iodine release from I_2@AR-2 in methanol. As shown in Fig. 11b, within 10 minutes, the iodine release efficiency reached 48%, increasing to 70% after 40 minutes. As the release progressed in Fig. 11b (inset), noticeable colour changes appeared in the crystals and the methanol solution. After 2 hours, the system reached equilibrium, with nearly 89% of the iodine released. However, the iodine release in methanol occurred gradually and steadily, suggesting that host–guest interactions controlled the process. I_2@AR-2 was washed with fresh methanol until all iodine was removed from its surface. It was then heated at 120 °C for 48 hours to ensure full iodine desorption, allowing it to be reused up to four times. With each cycle, the adsorption efficiency decreased by 4%, reaching a total of 14% reduction by the fourth cycle (Fig. 11c). These findings confirm that AR-2 is a durable and reusable material for iodine capture. It can further be verified by PXRD after each cycle that MOF AR-1 retains its crystallinity as shown in Fig. S13.†

3.4.8. Mechanism for iodine uptake. From SCXRD analysis, it is shown that the framework of AR-2 contains a significant number of aromatic rings and uncoordinated nitrogen atoms,

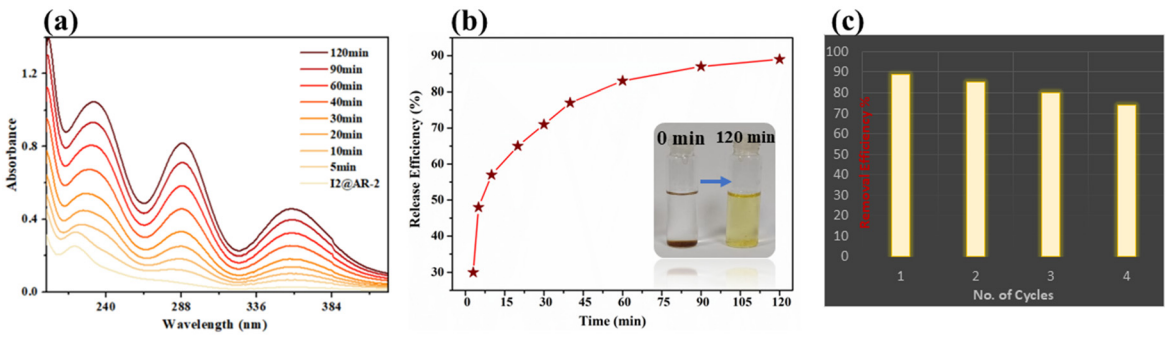

Fig. 11 (a) UV-vis spectra showing the time-dependent release of iodine from I_2@AR-2. (b) Release efficiency *vs.* time plot, with an inset showing the color change of the solution after 120 min. (c) Reusability performance of AR-2 over multiple adsorption–desorption cycles.

primarily due to the presence of H_4btc and Hata ligands. Literature reports suggest that free nitrogen atoms and aromatic rings enhance iodine adsorption.[84] This is primarily due to the π-electron-rich environment created by the H_4btc and Hata ligands, facilitating strong host–guest interactions (π···I) with iodine molecules. Since iodine (I_2) is a well-known σ* acceptor, it readily interacts with electron-rich π-systems, allowing efficient adsorption. Additionally, the uncoordinated nitrogen atoms (N_2 and N_4) in the Hata ligand possess lone pairs of electrons, making AR-2 a Lewis base. This allows the framework to engage in charge transfer (CT) interactions (n → σ)* with iodine, where free nitrogen atoms act as electron donors, while iodine molecules behave as Lewis acids. The abundance of uncoordinated nitrogen sites in the framework further enhances the formation of CT complexes with iodide anions, significantly improving iodine adsorption efficiency.[85] Furthermore, kinetic studies demonstrate that iodine adsorption follows a pseudo-second-order model, indicating that the process is governed by chemisorption. The synergistic effects of π···I interactions and charge-transfer complex formation significantly enhance the iodine uptake capacity of AR-2, establishing it as a promising adsorbent for iodine capture. This adsorption behavior can be preliminarily investigated using FTIR, PXRD, TGA, RAMAN, XPS, and SEM analyses. A comparison of the FTIR spectra of AR-2 and the iodine-loaded MOF in vapor, aqueous, and cyclohexane phases revealed significantly enhanced N–H stretching vibrations (3410–3350 cm^{-1}) in I_2@AR-2. The peak shifted from 3365 to 3332 cm^{-1} with increased iodine uptake, indicating noncovalent interactions between the amine groups of AR-2 and iodine.[86] The B, Q, and C–H bands of AR-2 at 1605, 1490, and 835 cm^{-1} shifted to 1595, 1488, and 830 cm^{-1}, respectively. The medium-strong bands corresponding to the triazole's C=N, C–N, and N–N stretching modes at 1640, 1430, and 1071 cm^{-1} shifted to 1689, 1481, and 1099 cm^{-1} (see Fig. S14a for details†). These observations suggest that iodine adsorption occurs at N–H and C–N units as well as aromatic rings in the AR-2 framework, similar to the behavior seen in Zn(tr)(OAc)-MOF.[87] This likely results from forming a charge transfer (CT) complex between AR-2 and iodine molecules.[88] Similarly, it can be concluded that before and after iodine adsorption in all phases, most of the peaks in the PXRD pattern remained at the same 2θ positions. However, the intensity of these peaks decreased, as shown in Fig. S14b.† The intensity and peak width changes suggest that the solid samples maintain their framework structure following iodine adsorption.[89] Thermogravimetric analysis (TGA) was employed to evaluate the iodine retention behavior of AR-2 (Fig. 12a).[90] The TGA profile of iodine-loaded AR-2 exhibited a significant weight loss between 70 °C and 500 °C. Sava *et al.*

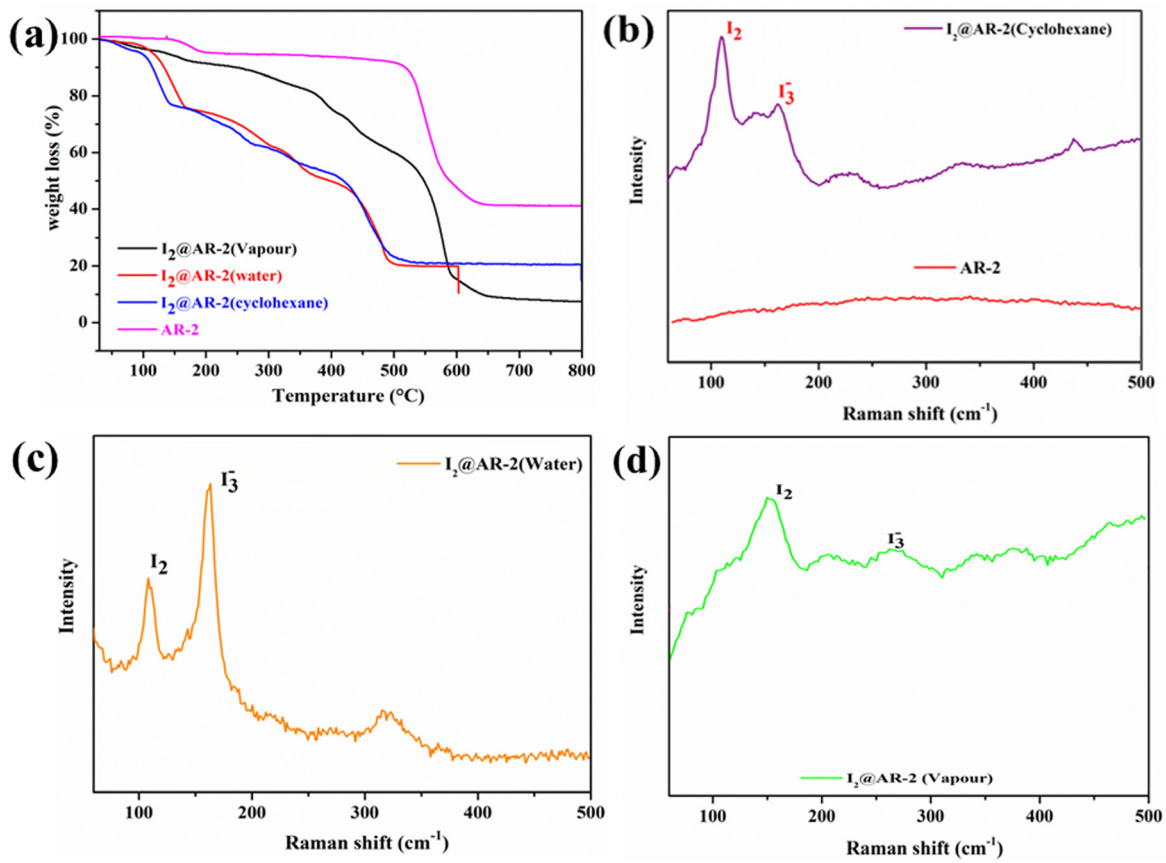

Fig. 12 (a) TGA analysis of AR-2 before and after iodine adsorption in different phases. (b) Raman spectra of AR-2 before and following iodine adsorption in cyclohexane solution, (c) in aqueous solution, and (d) in the vapor phase.

reported[91] that in this temperature range, not only I_2 but also iodide species such as I and HI were released along with a minor amount of CO_2. In contrast, the pristine AR-2 MOF remained stable under these conditions, with only the loss of coordinated water occurring near 200 °C, while the framework remained intact.[92] In the case of vapor-phase adsorption, the TGA profile of iodine-loaded AR-2 does not exhibit any distinct stepwise weight loss, indicating a more uniform desorption pattern. However, in aqueous and cyclohexane solution adsorption, a noticeable stepwise weight loss is observed, confirming that iodine desorption from AR-2 occurs in a gradual manner rather than as a single event, indicating that iodine interacts with the framework with moderate binding strength, neither too weak nor too strong. The observed weight loss is primarily attributed to the release of adsorbed iodine during heating. The iodine desorption was quantified as 190.4 wt% (aqueous solution), 182.8 wt% (vapor phase), and 135.6 wt% (cyclohexane solution), relative to the mass of AR-2. These values align closely with the iodine uptake capacity determined *via* gravimetric analysis. The remarkable iodine retention capacity of AR-2 can be attributed to robust charge-transfer interactions between the nitrogen-rich framework (acting as an electron donor) and the iodine species (acting as an electron acceptor), as reported in previous studies.[93,94] Raman and XPS spectroscopic techniques were used to identify the iodine species involved in the chemisorption process. The Raman spectra of iodine-adsorbed AR-2 in cyclohexane, aqueous, and vapor phases reveal two main vibrational bands around 110 cm^{-1} and 160 cm^{-1}, which correspond to the symmetric stretching of I_2 and I_3^-, respectively.[95,96] The presence of iodine at multiple sites within the open framework likely leads to the splitting and broadening of these bands. However, no distinct peak was observed in the Raman spectrum of AR-2 (Fig. 12b–d). Further XPS analysis before and after iodine adsorption (Fig. 13a) indicates that charge transfer occurs between the aromatic π-electrons of the MOF framework and the adsorbed iodine molecules, forming both I_2 and I_3^- species. The high-resolution I 3d XPS spectra (Fig. 13b–d) further support this charge-transfer interaction, which displays two distinct peaks at approximately 631.3 eV (I $3d_{3/2}$) and 619.8 eV (I $3d_{5/2}$). Deconvolution of these peaks reveals contributions from molecular iodine (631.5 eV and 619.8 eV) and triiodide ions (630.2 eV and 618.6 eV).[97,98] The chemisorption process is confirmed as the mechanism for forming the charge-transfer complex (CTC). In this process, the lone pair electrons (n) from the –N atom (Hata) interact with the antibonding (σ*) orbital of iodine, creating an initial outer charge-transfer complex (Hata-I_2). This outer complex then transitions into an inner charge-transfer complex ($Hata^+I^-$). As iodine molecules continue to adsorb, a polyiodide ion complex ($Hata^+I_3^-$) forms, as illustrated in the proposed mechanism in Fig. 14. To investigate morphological changes in the adsorbent, SEM images of AR-2 crystals were captured before and after iodine adsorption across all phases (Fig. 15a–d). Initially, AR-2 exhibited a smooth, well-defined block morphology with sharp edges. After iodine adsorption, considerable

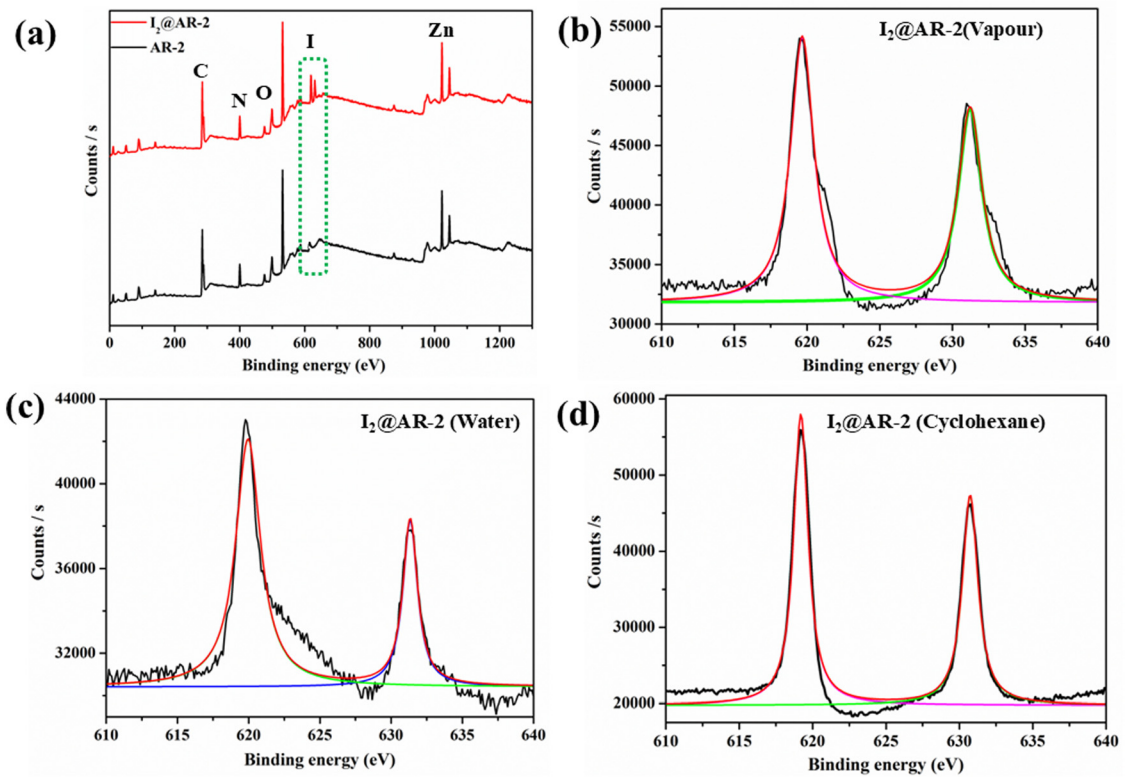

Fig. 13 (a) XPS analysis of AR-2 before and after iodine adsorption. (b–d) High-resolution XPS I 3d spectra in vapor, aqueous, and cyclohexane phases.

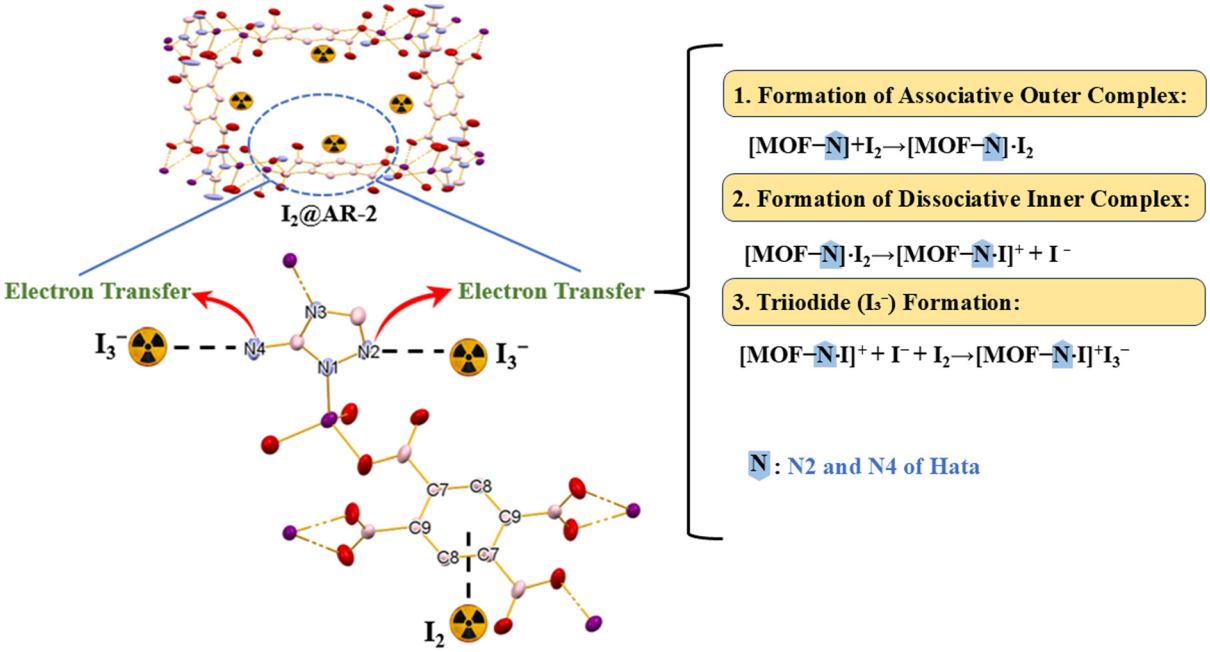

Fig. 14 A plausible mechanism for the formation of the CTC of AR-2 with iodine.

surface modifications were observed, indicating the iodine accumulation on the AR-2 surface, leading to a rough texture.[83] EDX (energy-dispersive X-ray spectroscopy) analysis before and after adsorption confirmed the incorporation of iodine into the AR-2 framework (Fig. 15e–h).

3.5. Dye adsorption

3.5.1. Specific adsorption of organic azo dyes. The as-synthesized AR-2 was evaluated for its adsorption capacity toward azo dye pollutants, specifically Bismarck Brown (BB) and Methyl Orange (MO), both recognized as environmental hazards. These dyes were selected as model azo dyes due to their contrasting charges. Extensive studies on MOFs have demonstrated selective dye adsorption, primarily governed by the structural and chemical attributes of the framework. Notably, MOFs with charged frameworks exhibit superior efficiency in adsorbing dyes from contaminated water.[99,100] However, there are very few reports where neutral frameworks have also been witnessed for good adsorption of naturally hazardous pollutants.[101] Moreover, AR-2 was stable in aqueous, acidic, and basic environments, making it a promising candidate for dye adsorption in aqueous systems. An exemplary experimental setup was created for the calibration

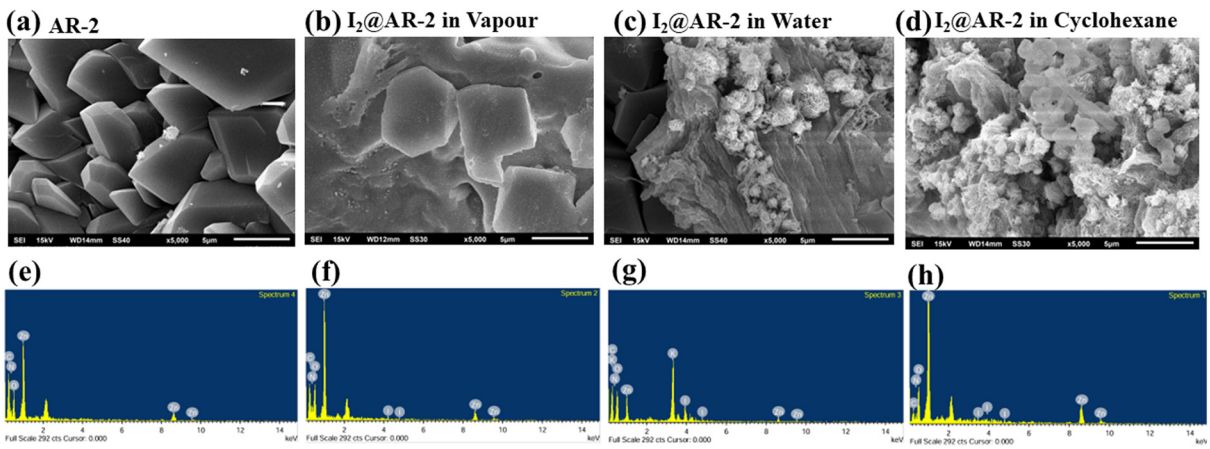

Fig. 15 SEM images of (a) pristine AR-2 and after iodine adsorption in (b) vapor, (c) water, and (d) cyclohexane. EDS spectra of (e) pristine AR-2 and (f–h) the iodinated MOF in different phases confirm iodine adsorption.

curve with different concentrations: 20, 15, 10, 5, and 2.5 ppm of Bismarck Brown and Methyl Orange dyes in distilled water (Fig. S15†).

The calibration curve was well known by measuring the absorbance at their respective maximum wavelengths using UV-vis spectroscopy. To evaluate the adsorption performance, 20 mg of synthesized AR-2 was introduced into 100 mL of 10 ppm aqueous dye solutions. A gradual decrease in dye concentration over time indicated rapid adsorption, highlighting the strong adsorption capacity of AR-2. The absorption peaks of BB and MO were observed at 470 nm and 464 nm, respectively. UV-vis spectra confirmed effective azo dye adsorption onto AR-2 (Fig. 16a & b). The removal efficiency, calculated using eqn (3),[102] showed that 64.01% of BB was adsorbed within 10 minutes. In contrast, MO removal reached 25.90% under the same conditions (Fig. 16c). Equilibrium was achieved after 40 minutes, with removal efficiencies of 93.75% and 86.66%, respectively, attributed to π–π stacking and cation–π interactions. The adsorption capacities for BB and MO were determined to be 49.84 and 25.01 mg g^{-1}, respectively, demonstrating the high efficiency of AR-2 in dye removal. Though selective dye adsorption is widely used for treating contaminated water, effectively separating organic azo dyes from a mixture remains a significant challenge.[103,104] To evaluate the potential of AR-2 for dye separation, the material was soaked in a BB/MO mixture, and the spectrum was analyzed using UV-visible spectroscopy. Since both dyes exhibit absorption in the 460–470 nm range, their peaks tend to overlap, resulting in a broadened band with a slight red shift, as shown in Fig. 16d. Notably, the results revealed that BB molecules were preferentially adsorbed over MO, demonstrating that AR-2 had the superior capacity to capture BB within a fixed time frame selectively. As depicted in Fig. S16a & b,† BB undergoes a significant color change from dark brown to clear. At the same time, MO transitions from orange to light yellow, indicating a reduction in dye concentration over time. The complete decolorization of BB suggests a higher adsorption efficiency than MO, which retains a faint yellow colour, reflecting its relatively lower adsorption.

The optimum adsorption conditions were explored by varying parameters such as pH and temperature. Adsorption experiments were conducted across a pH range of 2 to 14, using 0.1 M HCl and 0.1 M NaOH for adjustments. At low pH, adsorption decreases due to the interaction of H^+ ions with the cationic sites of BB. Conversely, the anionic pollutant can readily react with Na^+ ions at high pH, forming NaCl (Fig. 17a). The maximum adsorption capacity was achieved at pH 7, identified as the optimum pH.[105] The effect of temperature on adsorption was also studied within a range of 25 °C to 45 °C. As illustrated in Fig. 17b, the highest adsorption capacity was recorded at 25 °C, while the q_e value of AR-2 decreased noticeably at elevated temperatures.[106] Following the first adsorption cycle, the AR-2 crystals were recovered, washed sequentially with acetonitrile, methanol, and water, and dried in an oven at 70 °C for hours. The material maintained good adsorption efficiency for up to five cycles, but performance declined afterward due to sample leaching (Fig. 17c).[107] Despite this, the structural stability of AR-2 after the initial cycle was confirmed through PXRD analysis (Fig. S17†). The FTIR spectra show that AR-2 successfully adsorbs both Bismarck Brown (BB) and

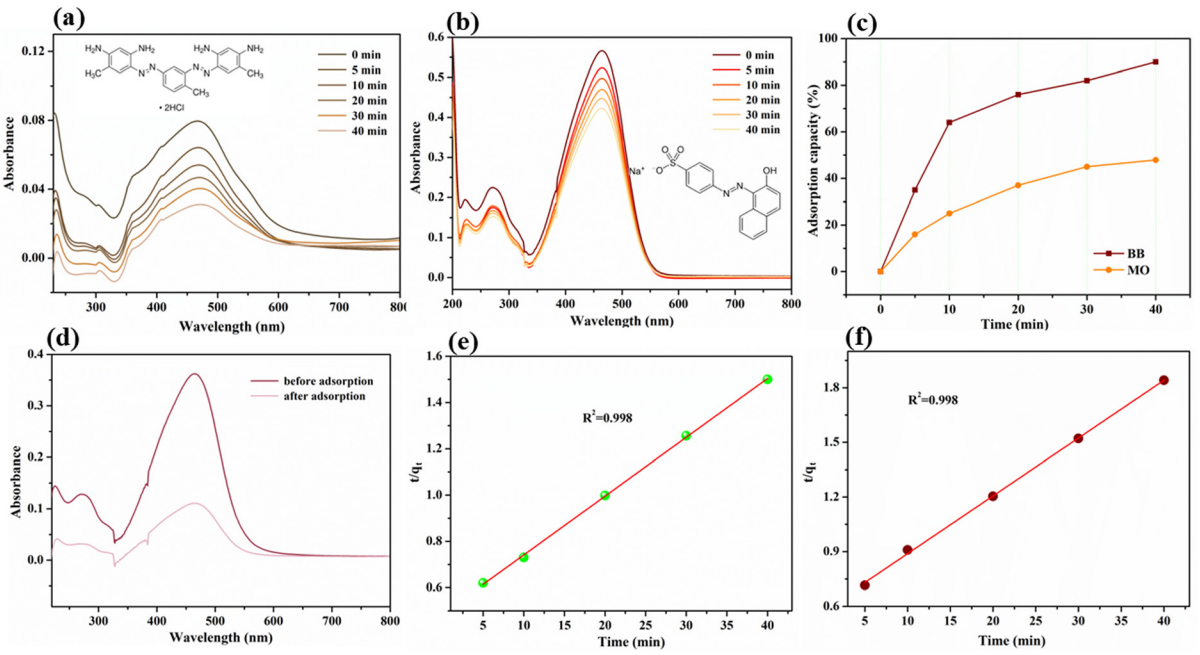

Fig. 16 UV-visible adsorption plots of azo dyes, *i.e.*, BB (a) and MO (b), recorded over time using AR-2 as the adsorbent. (c) Adsorption capacity (%) *vs.* time for BB and MO. (d) UV-vis spectra of the mixed dye before and following adsorption. (e and f) Kinetic fitting of the pseudo-second-order model for the adsorption of BB and MO onto AR-2.

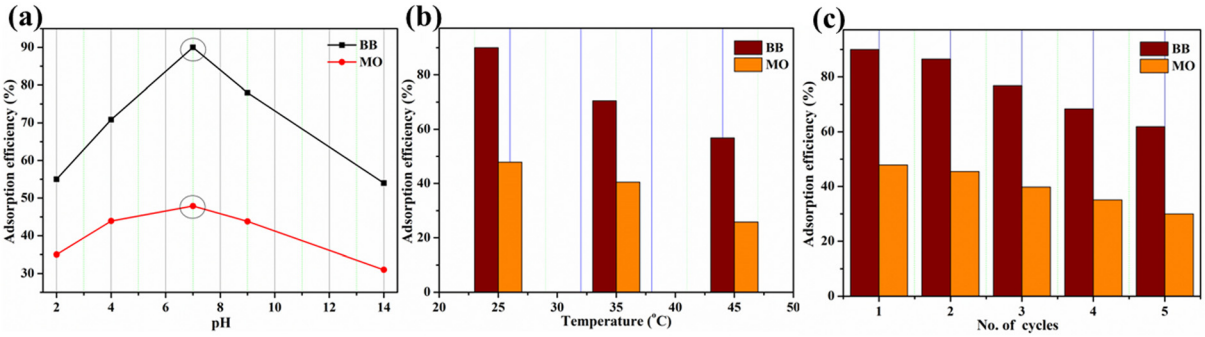

Fig. 17 (a) Effect of pH on the adsorption performance of AR-2 for BB and MO dyes. (b) Influence of temperature on the dye removal efficiency of AR-2. (c) Desorption efficiency of AR-2 across five successive cycles.

Methyl Orange (MO) dyes, as new peaks from the dyes appear in AR-2@MO and AR-2@BB. The retention of key spectral features after five adsorption–desorption cycles shows that the AR-2 framework remains unchanged, proving that it can be reused (Fig. S18 a and b†).

3.5.2. Adsorption kinetics of dyes. Kinetic analysis is crucial for understanding the dye adsorption mechanism. The pseudo-first-order and pseudo-second-order models were applied to investigate this, with kinetic parameters summarized in Table S8† using eqn (5) and (6). As depicted in Fig. S19,† the pseudo-first-order model shows a significant discrepancy between calculated and experimental adsorption capacities, indicating its inadequacy. In contrast, the pseudo-second-order model (Fig. 16e & f) exhibits excellent linearity with an R^2 value close to 1, suggesting that the adsorption process follows pseudo-second-order kinetics.

3.5.3. Plausible mechanism of dye adsorption. A plausible mechanism for dye adsorption by the AR-2 framework is illustrated in Fig. 18. Zeta potential analysis is a key technique for evaluating adsorption capacity and dye interactions.[108] The adsorption behavior of AR-2 was examined across a pH range of 2.0 to 14.0, as shown in Fig. S20.† The point of zero charge (pHpzc) of AR-2 was approximately 6.0, indicating that AR-2 remains electrically neutral at this pH. Under acidic conditions (pH < 6.0), protonation leads to a positively charged surface, whereas under alkaline conditions (pH > 6.0), hydroxide ions

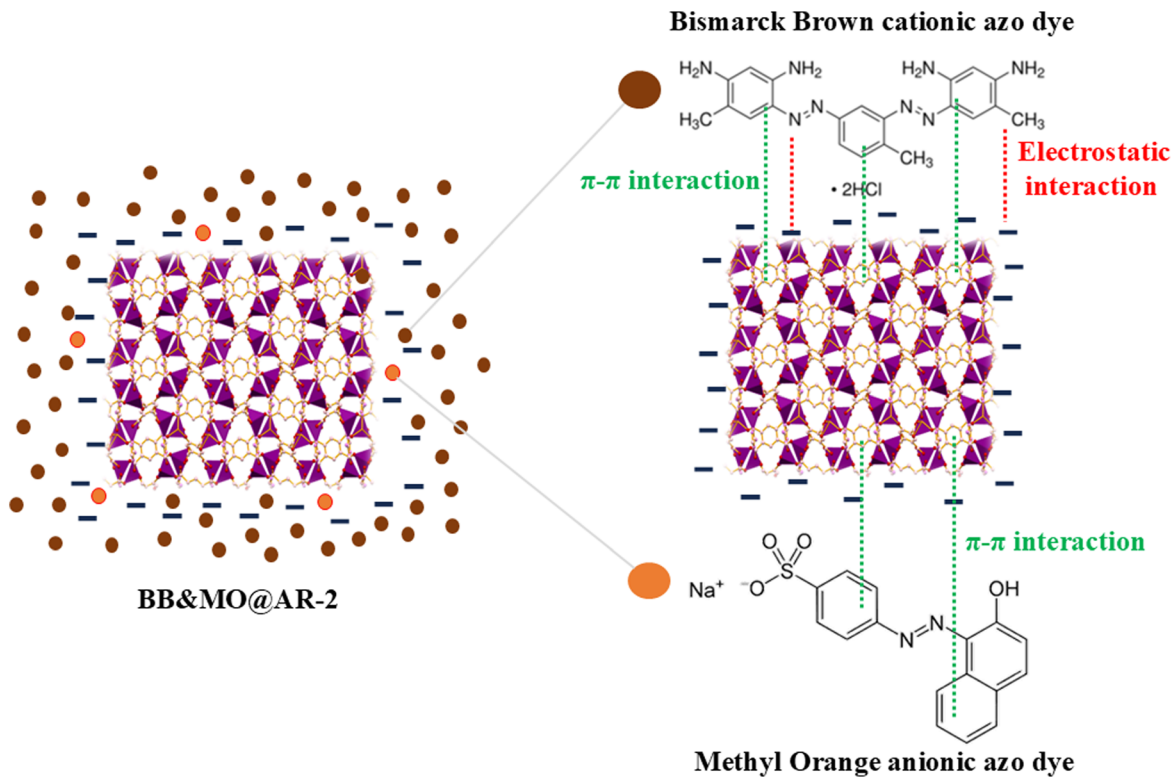

Fig. 18 Plausible cationic BB and anionic MO dye adsorption mechanism with AR-2.

accumulate, imparting a negative charge to AR-2. At neutral pH (pH = 7), the negatively charged AR-2 framework facilitates strong electrostatic interactions with cationic dye molecules (BB). Additionally, non-covalent interactions such as cation–π and π–π interactions significantly contribute to dye adsorption. The π-electron-rich framework of AR-2 enhances these interactions, promoting effective dye capture.[109] These additional interactions further enhance the absorption capacity of AR-2, making it a promising material for cationic dye removal. Furthermore, Methyl Orange (MO), a negatively charged dye, faces a distinct challenge when interacting with AR-2. Strong electrostatic repulsion between MO and the nucleophilic aromatic carboxylate ligands impedes effective adsorption. MO adsorption is primarily limited to π–π interactions, resulting in lower adsorption capacity than BB. The removal efficiency of AR-2 toward the dye was also compared with the other dye adsorbents in Table S9.† The BET surface area (3.050 $m^2 g^{-1}$) and pore volume (0.007 cc g^{-1}) values are quite low, indicating minimal internal porosity (Fig. S21†). Although the measured pore width is 2.769 nm (~27.69 Å), which is less than those of the dye molecules (Bismarck Brown ~17 × 10 × 9 Å; Methyl Orange ~14 × 6 × 4 Å), the two-fold interpenetrated structure significantly restricts internal pore accessibility. Thus, the effective adsorption of large azo dyes, such as Bismarck Brown and Methyl Orange, is primarily attributed to surface adsorption on the external surfaces, defects, or crystal boundaries of the framework, rather than true pore filling. This phenomenon of surface adsorption in low-porosity MOFs has been previously discussed in the literature.[110–112]

4. Conclusion

The synthesized 3D Zn-based MOF (AR-2) demonstrates potential practical applications in iodine uptake and dye adsorption. The interpenetrated structure, abundant donor sites, and high structural stability contribute to exceptional adsorption capacities under diverse conditions, including dry and humid environments for iodine. The ability of AR-2 to retain trapped iodine with minimal desorption and its selective uptake of hazardous dyes highlights its suitability for environmental cleanup processes. The straightforward synthesis of AR-2, combined with its excellent thermal and moisture stability, rapid adsorption kinetics, and high reusability with minimal performance degradation, positions it as a promising material for practical applications. Its potential extends to the efficient capture of radioiodine in nuclear facilities and the removal of hazardous dyes from industrial wastewater. This study highlights AR-2 as a highly effective and versatile adsorbent, offering significant prospects for sustainable waste management and environmental protection.

Data availability

Data will be made available on request.

Conflicts of interest

There are no conflicts to declare.

Acknowledgements

The authors acknowledge the USIF, AMU, Aligarh, for providing necessary research facilities. SAA gratefully thanks the UGC, New Delhi, for a non-NET fellowship.

References

1 N. Abas, A. Kalair and N. Khan, *Futures*, 2015, **69**, 31–49.
2 Y. Guan, J. Yan, Y. Shan, Y. Zhou, Y. Hang, R. Li, Y. Liu, B. Liu, Q. Nie and B. Bruckner, *Nat. Energy*, 2023, **8**, 304–316.
3 D. Welsby, J. Price, S. Pye and P. Ekins, *Nature*, 2021, **597**, 230–234.
4 K. Szulecki and I. Overland, *Nat. Energy*, 2023, **8**, 413–421.
5 A. Cho, *American Association for the Advancement of Science*, 2019.
6 H. Fell, A. Gilbert, J. D. Jenkins and M. Mildenberger, *Nat. Energy*, 2022, **7**, 25–29.
7 M. Poumadère, R. Bertoldo and J. Samadi, *Wiley Interdiscip. Rev. Clim. Change*, 2011, **2**, 712–727.
8 K. Menyah and Y. Wolde-Rufael, *Energy Policy*, 2010, **38**, 2911–2915.
9 G. Steinhauser, *Environ. Sci. Technol.*, 2014, **48**, 4649–4663.
10 Y. Hao, Z. Tian, C. Liu and C. Xiao, *Front. Chem.*, 2023, **11**, 1122484.
11 Z. Tian, T.-S. Chee, X. Zhang, L. Lei and C. Xiao, *Chem. Eng. J.*, 2021, **412**, 128687.
12 K. Kang, S. Liu, M. Zhang, L. Li, C. Liu, L. Lei, X. Dai, C. Xu and C. Xiao, *Adv. Funct. Mater.*, 2022, **32**, 2208148.
13 W. Xie, D. Cui, S.-R. Zhang, Y.-H. Xu and D.-L. Jiang, *Mater. Horiz.*, 2019, **6**, 1571–1595.
14 T. J. Robshaw, J. Turner, S. Kearney, B. Walkley, C. A. Sharrad and M. D. Ogden, *SN Appl. Sci.*, 2021, **3**, 1–15.
15 R. M. Grossi, *American Association for the Advancement of Science*, 2021.
16 M. Nadesan, *Fukushima and the Privatization of Risk*, Springer, 2013.
17 M. A. Greer, G. Goodman, R. C. Pleus and S. E. Greer, *Environ. Health Perspect.*, 2002, **110**, 927–937.
18 M. Schlumberger, L. Lacroix, D. Russo, S. Filetti and J.-M. Bidart, *Nat. Clin. Pract. Endocrinol. Metab.*, 2007, **3**, 260–269.
19 S. Abubakar, T. Skorjanc, D. Shetty and A. Trabolsi, *ACS Appl. Mater. Interfaces*, 2021, **13**, 14802–14815.
20 A. Hassan, A. Alam, M. Ansari and N. Das, *Chem. Eng. J.*, 2022, **427**, 130950.
21 A. Ghosh and G. Das, *Microporous Mesoporous Mater.*, 2020, **297**, 110039.

22 M. T. Yagub, T. K. Sen and H. M. Ang, *Water, Air, Soil Pollut.*, 2012, **223**, 5267–5282.
23 K. Chinoune, K. Bentaleb, Z. Bouberka, A. Nadim and U. Maschke, *Appl. Clay Sci.*, 2016, **123**, 64–75.
24 K. Wang, C. Li, Y. Liang, T. Han, H. Huang, Q. Yang, D. Liu and C. Zhong, *Chem. Eng. J.*, 2016, **289**, 486–493.
25 D. Rawat, R. S. Sharma, S. Karmakar, L. S. Arora and V. Mishra, *Ecotoxicol. Environ. Saf.*, 2018, **148**, 528–537.
26 K. Yamjala, M. S. Nainar and N. R. Ramisetti, *Food Chem.*, 2016, **192**, 813–824.
27 M. J. Greenwald, A. M. Redding and F. S. Cannon, *Water Res.*, 2015, **68**, 784–792.
28 T. Yao, S. Guo, C. Zeng, C. Wang and L. Zhang, *J. Hazard. Mater.*, 2015, **292**, 90–97.
29 F. Liu, Z. Guo, H. Ling, Z. Huang and D. Tang, *Microporous Mesoporous Mater.*, 2016, **227**, 104–111.
30 S. Sarkar, P. Chakraborty and R. Bandopadhyay, *Comb. Appl. Physico-Chemical Microbiol. Process. Ind. Effl. Treat. Plant*, 2020, pp. 47–63.
31 I. Safarik, P. Lunackova, E. Mosiniewicz-Szablewska, F. Weyda and M. Safarikova, *Wood Research and technology Holzforschung*, 2007, **61**, 3.
32 Y. Li, C. Gao, J. Jiao, J. Cui, Z. Li and Q. Song, *ACS Omega*, 2021, **6**, 33961–33968.
33 K. M. A. Qasem, M. Y. Khan, S. A. Akmal, H. A. M. Saleh, M. Mehtab, M. Shahid, M. A. S. Salem, M. M. A. Khan, Y. S. A. Ghanem and A. Malik, *J. Water Process Eng.*, 2025, **69**, 106569.
34 S. A. Akmal, M. Khalid, M. S. Ahmad, M. Shahid and M. Ahmad, *Cryst. Growth Des.*, 2024, **24**, 7173–7193.
35 F. Vakil, M. S. Ahmad, M. Kumar, A. Ansari, M. Shahid and M. Ahmad, *CrystEngComm*, 2023, **25**, 2280–2297.
36 M. Zeeshan, M. Y. Khan, R. Khan, M. Mehtab and M. Shahid, *CrystEngComm*, 2024, **26**, 5489–5517.
37 S. Mukherjee, S. Dutta, Y. D. More, S. Fajal and S. K. Ghosh, *Dalton Trans.*, 2021, **50**, 17832–17850.
38 P. Wang, C. N. Moorefield, M. Panzer and G. R. Newkome, *Chem. Commun.*, 2005, 465–467.
39 L.-Y. Wang, Y. Yang, K. Liu, B.-L. Li and Y. Zhang, *Cryst. Growth Des.*, 2008, **8**, 3902–3904.
40 J.-D. Lin, Y.-H. Li, J.-G. Xu, F.-K. Zheng, G.-C. Guo, R.-X. Lv, W.-C. He, Z.-N. Huang and J.-F. Liu, *J. Solid State Chem.*, 2018, **265**, 42–49.
41 Z. Chen, X. Li and F. Liang, *J. Solid State Chem.*, 2008, **181**, 2078–2086.
42 B. Li, X. Dong, H. Wang, D. Ma, K. Tan, S. Jensen, B. J. Deibert, J. Butler, J. Cure and Z. Shi, *Nat. Commun.*, 2017, **8**, 485.
43 W. C. Hamilton and J. A. Ibers, *International Tables for X-ray Crystallography*, Kynoch Press, Birmingham, England, 1974, vol. IV, pp. 275–281.
44 *SMART & SAINT, Software Reference Manuals, Version 6.45*, Bruker Analytical X-ray Systems, Inc., Madison, 2003.
45 A.-D. A. C. Sadabs, *Acta Crystallogr., Sect. A:Found. Crystallogr.*, 1995, **51**, 33.
46 G. M. Sheldrick, *Sheldrick, SADABS, software for empirical absorption correction, Ver. 2.05*, University of Göttingen, Göttingen, Germany, 2002.
47 L. J. Bourhis, O. V. Dolomanov, R. J. Gildea, J. A. K. Howard and H. Puschmann, *J. Appl. Crystallogr.*, 2015, **71**, 59–75.
48 J.-S. Qin, S. Yuan, Q. Wang, A. Alsalme and H.-C. Zhou, *J. Mater. Chem. A*, 2017, **5**, 4280–4291.
49 L. Yang, D. R. Powell and R. P. Houser, *Dalton Trans.*, 2007, 955–964.
50 L.-W. Lee, Y.-C. Kao, M.-Y. Chung, B.-C. Chang, G.-H. Lee, S.-M. Peng, C.-M. Wang, Y.-H. Liu, S.-L. Lee and K.-L. Lu, *Dalton Trans.*, 2019, **48**, 1950–1954.
51 A. W. Addison, T. N. Rao, J. Reedijk, J. van Rijn and G. C. Verschoor, *J. Chem. Soc., Dalton Trans.*, 1984, 1349–1356.
52 H. Vahrenkamp, *Acc. Chem. Res.*, 1999, **32**, 589–596.
53 N. E. Brese, *Acta Crystallogr., Sect. B:Struct. Sci.*, 1991, **47**, 192.
54 J. Gao, N. Wang, X. Xiong, C. Chen, W. Xie, X. Ran, Y. Long, S. Yue and Y. Liu, *CrystEngComm*, 2013, **15**, 3261–3270.
55 E.-C. Yang, X.-Y. Zhang, X.-G. Wang, Z.-Y. Liu and X.-J. Zhao, *Polyhedron*, 2013, **53**, 208–214.
56 Y.-S. Shi, Q. Yu, J.-W. Zhang and G.-H. Cui, *CrystEngComm*, 2021, **23**, 1604–1615.
57 P.-X. Yin, J.-K. Cheng, Z.-J. Li, L. Zhang, Y.-Y. Qin, J. Zhang and Y.-G. Yao, *Inorg. Chem.*, 2009, **48**, 10859–10861.
58 D. Majumdar, A. Frontera, S. Roy and D. Sutradhar, *ACS Omega*, 2023, **9**, 1786–1797.
59 P. Deepa, R. Vijay Solomon, S. Vedha Angeline, P. Kolandaivel and P. Venuvanalingam, *Mol. Phys.*, 2014, **112**, 3195–3205.
60 H. A. M. Saleh, S. Khan, M. Kumar, A. Ansari, M. Shahid, F. Sama, K. M. A. Qasem, M. Y. Khan, M. Mehtab and M. Ahmad, *Inorg. Chem.*, 2023, **63**, 329–345.
61 J.-D. Lin, Z.-J. Huang, Y.-P. Xie and Q.-L. Li, *J. Mol. Struct.*, 2015, **1083**, 163–167.
62 S. Hassen, Y. Arfaoui, T. Steenhaut, Y. Filinchuk, A. Klein and H. Chebbi, *Inorg. Chim. Acta*, 2023, **557**, 121664.
63 F. A. Almeida Paz and J. Klinowski, *Inorg. Chem.*, 2004, **43**, 3882–3893.
64 B. Liu, H.-J. Feng, Z.-H. Zhang, L. Xu and H. Jiao, *J. Mol. Struct.*, 2015, **1098**, 240–245.
65 L. Lu, J. Wang, S. Zhou, Y. Zhong, Y. Sun, X. Wu, A. Singh and A. Kumar, *Inorg. Chim. Acta*, 2020, **508**, 119647.
66 Y. Li, N. Hao, Y. Lu, E. Wang, Z. Kang and C. Hu, *Inorg. Chem.*, 2003, **42**, 3119–3124.
67 S. Hassen, Y. Arfaoui, K. Robeyns, T. Steenhaut, Y. Filinchuk, A. Klein and H. Chebbi, *J. Coord. Chem.*, 2022, **75**, 908–924.
68 M. Yin, C. Wu, X. Yang, Y. Wang and Y. Fan, *Synth. React. Inorg., Met.-Org., Nano-Met. Chem.*, 2010, **40**, 798–804.
69 S. H. Sumrra, W. Zafar, M. L. Asghar, F. Mushtaq, M. A. Raza, M. F. Nazar, M. A. Nadeem, M. Imran and S. Mumtaz, *J. Mol. Struct.*, 2021, **1238**, 130382.

70 I. Matulkova, I. Němec, K. Teubner, P. Němec and Z. Mička, *J. Mol. Struct.*, 2008, **873**, 46–60.
71 Y. Zhang, J. Zhou, X. Chen, Q. Feng and W. Cai, *J. Alloys Compd.*, 2019, **777**, 109–118.
72 N. U. D. Mir, M. S. Ahmad, S. Khan, M. Y. Khan, F. Vakil, S. Saraswat and M. Shahid, *Inorg. Chem. Commun.*, 2022, **146**, 110046.
73 M. Y. Khan, A. Husain, D. K. Mahajan, M. Muaz, M. Shahid, M. Zeeshan, F. Sama and S. Ahmad, *Dalton Trans.*, 2024, **53**, 7477–7497.
74 M. Díaz-García, A. Mayoral, I. Díaz and M. Sánchez-Sánchez, *Cryst. Growth Des.*, 2014, **14**, 2479–2487.
75 R. T. Jubin, D. M. Strachan and N. R. Soelberg.
76 F. C. Küpper, M. C. Feiters, B. Olofsson, T. Kaiho, S. Yanagida, M. B. Zimmermann, L. J. Carpenter, G. W. Luther III, Z. Lu and M. Jonsson, *Angew. Chem., Int. Ed.*, 2011, **50**, 11598–11620.
77 Y. Lin, X. Jiang, S. T. Kim, S. B. Alahakoon, X. Hou, Z. Zhang, C. M. Thompson, R. A. Smaldone and C. Ke, *J. Am. Chem. Soc.*, 2017, **139**, 7172–7175.
78 A. Gogia, P. Das and S. K. Mandal, *ACS Appl. Mater. Interfaces*, 2020, **12**, 46107–46118.
79 Z. Guo, P. Sun, X. Zhang, J. Lin, T. Shi, S. Liu, A. Sun and Z. Li, *Chem. – Asian J.*, 2018, **13**, 2046–2053.
80 S. P. Tripathy, R. Acharya, M. Das, R. Acharya and K. Parida, *Mater. Today: Proc.*, 2020, **30**, 289–293.
81 A. Sarkar, A. Adhikary, A. Mandal, T. Chakraborty and D. Das, *Cryst. Growth Des.*, 2020, **20**, 7833–7839.
82 J. Jeromenok and J. Weber, *Langmuir*, 2013, **29**, 12982–12989.
83 Y. Zhao, N. Zhang, Y. Wang, F. Y. Bai, Y. H. Xing and L. X. Sun, *Inorg. Chem. Front.*, 2021, **8**, 1736–1746.
84 P. Chen, X. He, M. Pang, X. Dong, S. Zhao and W. Zhang, *ACS Appl. Mater. Interfaces*, 2020, **12**, 20429–20439.
85 S. Xiong, X. Tang, C. Pan, L. Li, J. Tang and G. Yu, *ACS Appl. Mater. Interfaces*, 2019, **11**, 27335–27342.
86 P.-S. Huang, C.-H. Kuo, C.-C. Hsieh and Y.-C. Horng, *Chem. Commun.*, 2012, **48**, 3227–3229.
87 J. Qin, W. Zhang, Y. Chen, R. Liu and Y. Fan, *Environ. Sci. Pollut. Res.*, 2021, **28**, 28797–28807.
88 T. Hasell, M. Schmidtmann and A. I. Cooper, *J. Am. Chem. Soc.*, 2011, **133**, 14920–14923.
89 A. Beheshti, E. S. M. Fard, M. Kubicki, P. Mayer, C. T. Abrahams and S. E. Razatofighi, *CrystEngComm*, 2019, **21**, 251–262.
90 X. Pan, C. Ding, Z. Zhang, H. Ke and G. Cheng, *Microporous Mesoporous Mater.*, 2020, **300**, 110161.
91 D. F. Sava, K. W. Chapman, M. A. Rodriguez, J. A. Greathouse, P. S. Crozier, H. Zhao, P. J. Chupas and T. M. Nenoff, *Chem. Mater.*, 2013, **25**, 2591–2596.
92 X. Pan, X. Qin, Q. Zhang, Y. Ge, H. Ke and G. Cheng, *Microporous Mesoporous Mater.*, 2020, **296**, 109990.
93 Y.-E. Jung, S.-W. Kang and M.-S. Yim, *Ind. Eng. Chem. Res.*, 2021, **60**, 5964–5975.
94 W. Huang, Y. Jiang, X. Li, X. Li, J. Wang, Q. Wu and X. Liu, *ACS Appl. Mater. Interfaces*, 2013, **5**, 8845–8849.
95 G. Massasso, M. Rodríguez-Castillo, J. Long, A. Grandjean, B. Onida, Y. Guari, C. Guerin and J. Larionova, *J. Mater. Chem. A*, 2015, **3**, 179–188.
96 Z.-J. Li, Z. Yue, Y. Ju, X. Wu, Y. Ren, S. Wang, Y. Li, Z.-H. Zhang, X. Guo and J. Lin, *Inorg. Chem.*, 2020, **59**, 4435–4442.
97 Z. Yan, Y. Yuan, Y. Tian, D. Zhang and G. Zhu, *Angew. Chem.*, 2015, **127**, 12924–12928.
98 X. Qian, Z.-Q. Zhu, H.-X. Sun, F. Ren, P. Mu, W. Liang, L. Chen and A. Li, *ACS Appl. Mater. Interfaces*, 2016, **8**, 21063–21069.
99 K. Maity, T. Kundu, R. Banerjee and K. Biradha, *CrystEngComm*, 2015, **17**, 4439–4443.
100 Y.-Y. Jia, Y.-H. Zhang, J. Xu, R. Feng, M.-S. Zhang and X.-H. Bu, *Chem. Commun.*, 2015, **51**, 17439–17442.
101 S. K. Konavarapu, A. Goswami, A. G. Kumar, S. Banerjee and K. Biradha, *Inorg. Chem. Front.*, 2019, **6**, 184–191.
102 M. S. Khan, M. Khalid, M. S. Ahmad, M. Shahid and M. Ahmad, *Dalton Trans.*, 2019, **48**, 12918–12932.
103 M. Z. Wu, J. Y. Shi, P. Y. Chen, L. Tian and J. Chen, *Inorg. Chem.*, 2019, **58**, 3130–3136.
104 C. Liu, L.-Q. Yu, Y.-T. Zhao and Y.-K. Lv, *Microchim. Acta*, 2018, **185**, 1–12.
105 M. N. Ahamad, M. S. Khan, M. Shahid and M. Ahmad, *Dalton Trans.*, 2020, **49**, 14690–14705.
106 K. Iman, M. Shahid, M. S. Khan, M. Ahmad and F. Sama, *CrystEngComm*, 2019, **21**, 5299–5309.
107 U. Patel, B. Parmar, P. Patel, A. Dadhania and E. Suresh, *Mater. Chem. Front.*, 2021, **5**, 304–314.
108 H. A. M. Saleh, I. Mantasha, K. M. A. Qasem, M. Shahid, M. N. Akhtar, M. A. AlDamen and M. Ahmad, *Inorg. Chim. Acta*, 2020, **512**, 119900.
109 G.-Q. Wang, J.-F. Huang, X.-F. Huang, S.-Q. Deng, S.-R. Zheng, S.-L. Cai, J. Fan and W.-G. Zhang, *Inorg. Chem. Front.*, 2021, **8**, 1083–1092.
110 K. S. Park, Z. Ni, A. P. Côté, J. Y. Choi, R. Huang, F. J. Uribe-Romo, H. K. Chae, M. O'Keeffe and O. M. Yaghi, *Proc. Natl. Acad. Sci. U. S. A.*, 2006, **103**, 10186–10191.
111 B. L. Tran, H.-Y. Chin, B. K. Chang and A. S. T. Chiang, *Microporous Mesoporous Mater.*, 2019, **277**, 149–153.
112 G. Férey, C. Mellot-Draznieks, C. Serre, F. Millange, J. Dutour, S. Surblé and I. Margiolaki, *Science*, 2005, **309**, 2040–2042.